Earth and Planetary Science Letters 549 (2020) 116539

Contents lists available at ScienceDirect

Earth and Planetary Science Letters

www.elsevier.com/locate/epsl

The architecture of intrusions in magmatic mush

Alexandre Carrara [a,*], Alain Burgisser [a], George W. Bergantz [b]

[a] Univ. Grenoble Alpes, Univ. Savoie Mont Blanc, CNRS, IRD, IFSTTAR, ISTerre, 38000 Grenoble, France
[b] Department of Earth and Space Sciences, Box 351310, University of Washington, Seattle, WA 98195, USA

ARTICLE INFO

Article history:
Received 16 January 2020
Received in revised form 30 June 2020
Accepted 14 August 2020
Available online xxxx
Editor: H. Handley

Keywords:
mush
magma
intrusion
density contrast
CDF-DEM
granular mechanics

ABSTRACT

Magmatic reservoirs located in the upper crust have been shown to result from the repeated intrusions of new magmas, and spend much of the time as a crystal-rich mush. The geometry of the intrusion of new magmas may greatly affect the thermal and compositional evolution of the reservoir. Despite advances in our understanding of the physical processes that may occur in a magmatic reservoir, the resulting architecture of the composite system remains poorly constrained. Here we performed numerical simulations coupling a computational fluid dynamics and a discrete element method in order to illuminate the geometry and emplacement dynamics of a new intrusion into mush and the relevant physical parameters controlling it. Our results show that the geometry of the intrusion is to first order controlled by the density contrast that exists between the melt phases of the intrusion and resident mush rather than the bulk density contrast as is usually assumed. When the intruded melt is denser than the host melt, the intrusion pounds at the base of the mush and emplaced as a horizontal layer. The occurrence of Rayleigh-Taylor instability leading to the rapid ascent of the intruded material through the mush was observed when the intruded melt was lighter than the host one and was also unrelated to the bulk density contrast. In the absence of density contrasts between the two melt phases, the intrusion may fluidize the host crystal network and slowly ascend through the mush. The effect of the viscosity contrast between the intruded and host materials was found to have a lesser importance on the architecture of intrusions in a mush. Analyzing the eruptive sequence of well documented eruptions involving an intrusion as the trigger shows a good agreement with our modeling results, highlighting the importance of specifically considering granular dynamics when evaluating magmas and mush physical processes.

1. Introduction

Evidence for injections of new magmas, also called recharge events, are ubiquitous in magmatic systems (Wiebe, 2016). They are inferred to cause the formation of long-lived, supersolidus magmatic reservoirs located in the upper crust (e.g. Annen et al., 2015, 2006; Dufek and Bergantz, 2005; Karakas et al., 2017). Together with the thermal structure of the upper crust and the frequency of recharge, the geometry and mode of emplacement of the intruded magma was also identified as having a crucial effect on the long-term evolution of igneous bodies (Annen et al., 2015). Diverse evidence supports the view that magmatic reservoirs reside most time in a mush state that is frequently disturbed by injection of new magmas (e.g. Bachmann and Huber, 2016; Cashman et al., 2017, and references therein). A magmatic mush is a crystal-rich magma in which crystals are in close and sometimes frictional contacts, forming a semi-rigid framework where stress is transmitted by force chains (Bergantz et al., 2017). As a result, mushes transition between crystal-rich suspensions to a 'lock-up' state that inhibits the ability of the magma to erupt.

The injection of hotter magma into a cooler host has been suggested as a means to trigger volcanic eruptions (e.g. Caricchi et al., 2014) and the intrusion style plays a fundamental role in the way mush rejuvenates (process of recycling the mush to generate an eruptible magma) prior to eruption (Parmigiani et al., 2014, and references therein). Several scenarios assume that the intruder is emplaced as sills at the base of the mush (underplating), and rejuvenate it by supplying heat but no mass except possibly exsolved volatiles (Bachmann and Bergantz, 2006; Bergantz, 1989; Burgisser and Bergantz, 2011; Couch et al., 2001; Huber et al., 2011). Other scenarios consider that the injected magma may penetrate the mush, producing various degrees of mixing with the resident mush depending on its buoyant acceleration (e.g. Bergantz and Breidenthal, 2001; Koyaguchi and Kaneko, 2000; Weinberg and Leitch, 1998). Whether an intrusion generates extensive mass transfer, or is limited to thermal exchanges between an underplated intruder and a host mush is thus a key element shaping the outcome of

* Corresponding author.
E-mail address: carrara.alexandre.univ@gmail.com (A. Carrara).

https://doi.org/10.1016/j.epsl.2020.116539
0012-821X/

open-system events. A major obstacle to our current understanding of the formation and evolution of igneous bodies is that little is known about the architecture of intrusions and controlling physical parameters.

Traditionally, mush rejuvenation scenarios have been based on the results of experiments performed with pure fluids mimicking the bulk physical properties (density and viscosity) of the magmas (e.g. Huppert et al., 1986; Jellinek and Kerr, 1999; Snyder and Tait, 1995). Mush dynamics, however, differs from that of pure fluids because of the complex rheological feedbacks between melt and crystals. An essential physical process is that melt and crystals may experience relative motions. Numerical simulations explicitly accounting for such decoupled motions as well as the building and destruction of force chains between crystals have revealed that the local injection of pure melt of the same density and viscosity as the mush interstitial melt easily fluidizes, penetrates, and partially mixes with the overlying mush if it is sufficiently vigorous. This local unlocking of a mush shows that the conditions for efficient mass transfer and mixing are easier to achieve than previously thought. Conversely, it is adding constraints on rejuvenation scenarios based on the emplacement of an underlying mafic gravity current (e.g. Bachmann and Bergantz, 2006; Burgisser and Bergantz, 2011) by suggesting that underplating may require contrasts in densities and/or viscosities to hinder fluidization.

Our capacity to interpret the various natural expressions of open-system events, such as eruptive products containing both the intruded magma and the resident mush, is hindered by our partial understanding of the architectural end-members of these events, such as fluidization or underplating. To characterize the geometry and emplacement styles of intrusion events into a residing mush, we performed numerical simulations using a combination of fluid mechanics and discrete elements (Bergantz et al., 2015; Schleicher et al., 2016; Schleicher and Bergantz, 2017; Carrara et al., 2019; McIntire et al., 2019; Burgisser et al., 2020). As the dissimilarities between the density and viscosity of the two melts require special attention to better characterize the end-member cases of open-system events, we explored how these parameters condition the dynamics of the intruded material when injected into a mush. We first introduce the numerical model and the dimensionless parameters controlling recharge dynamics that are varied in the simulations. Results of numerical simulations involving magmas of contrasting physical properties are then presented in the framework of the dimensionless parameters. Finally, we relate our results to well-documented cases of eruptions triggered by an intrusion event.

2. Method

In order to characterize the geometry and emplacement mechanism of intrusion in mush accounting for granular dynamics, we performed Computational-Fluid-Dynamic and Discrete-Element-Method (CFD-DEM) numerical simulations by using the MFIX-DEM software (https://mfix.netl.doe.gov/). The coupled melt-crystal flow is computed solving the mass and momentum conservation equations with a finite volume method for the melt, and using a discrete model including explicitly of particle interactions for the crystals. Details about the theory and implementation of the model can be found in Garg et al. (2012), Syamlal (1998), Syamlal et al. (1993), and validation of the DEM approaches in Garg et al. (2012) and Li et al. (2012) (see supplementary information 1 for an overview of the numerical model, a discussion about its validity, and a list of the equations we used).

The computational domain is a 3D medium of $1.6 \times 0.8 \times 0.05$ m (length $\times$ height $\times$ width; $128 \times 64 \times 4$ cells) filled with a resident mush (Fig. 1). This geometry also allowed us to populate the mush with mm-size particles, ensuring that the dimensionless numbers describing the nature of the flow and the contrasts between the physical properties of the two magmas cover the ranges found in nature (see Supplementary information 1). We will show a posteriori that our particle bed behaves identically to a bed twice as thick (Bergantz et al., 2015). Our runs are thus representative of an open system event despite the small size of the domain compared to a natural system. We used such geometry instead of a two dimensional one to ensure that the build-up and breaking of force chains have a sufficient degree of freedom in space to replicate best the mechanics of the granular phase. We created a mush layer of ~0.3 m height with an initial crystal volume fraction of ~0.64 by simulating the settling of the particles in a vacuum and positioning them at the base of the domain. We used the same density for all particles ($\rho_p = 3300$ kg m^{-3}) and three different diameters (4.5, 5, and 5.5 mm, constituting 25, 50, and 25% of the total number of particles, respectively) to avoid artificial self-organization of the particles in a regular lattice. All simulations use the same initial particle bed. A crystal-free magma is injected at the base of the mush layer with a superficial vertical velocity, U_{inj}, through an inlet having a width, W_{inj}. The density and the viscosity of the injected melt are kept constant between all the simulations ($\rho_i = 2500$ kg m^{-3}; $\eta_i = 1$ Pa s, see Table 1, Table 2 for the list of the parameters kept constant). We used a conduit of 3.2 cm in height to supply the inlet to ensure that the intruder enters the mush as a Poiseuille flow. At the top of the domain, we used a pressure outflow boundary condition to ensure the overall mass conservation within the entire domain, which is consistent with an open-system event. The boundary conditions at the front and back of the domain are cyclical, which means that the intruder corresponds to a dyke having one infinite dimension. All the other boundary conditions are non-slip walls (Fig. 1). To maintain constant values of melt density and viscosity during the runs (and hence constant density and viscosity contrasts), thermal effects are ignored. This is consistent with the small dimensions of the computational domain that ensure run times shorter than those allowing significant heat exchanges (the characteristic time to diffuse the heat over 1 cell is ~400 s and the longest simulations lasts ~500 s). In each fluid cell, the local melt density and viscosity depend linearly on the two end-member properties and on their respective concentrations, which are tracked by a transport equation (see Supplementary material 1).

We performed simulations by varying the density and viscosity of the host melt. In order to compare simulations, we used dimensionless quantities to scale the effects of the contrasts in densi-

Table 1
List of symbols and their meaning.

Symbol (unit)	Definition
At	Atwood number between the two melts
At_b	Bulk Atwood number
E (Pa)	Particle Young modulus
H_{bed} (m)	Particle bed thickness
H (m)	Intruded layer maximum height above the inlet
H^*	Dimensionless height of the intruded volume
t^*	Reduced time
U_{inj} (m s^{-1})	Injection superficial velocity
U_{mf} (m s^{-1})	Minimum fluidization superficial velocity
U^*	Dimensionless injection velocity
W_{inj} (m)	Injection width
η_i (Pa s)	Intruder melt dynamic viscosity
η_h (Pa s)	Host melt dynamic viscosity
η^*	Melts dynamic viscosity ratio
μ	Particle friction coefficient
ρ_h (kg m^{-3})	Host melt density
ρ_i (kg m^{-3})	Intruder melt density
ρ_p (kg m^{-3})	Density of the particles
σ	Poisson coefficient
Φ	Solid volume fraction

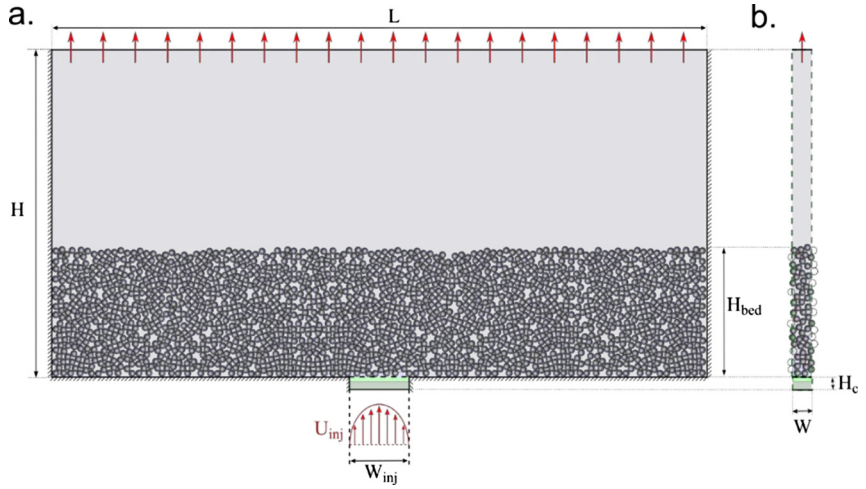

Fig. 1. Simulations initial condition. [A] The drawing represents the computational domain viewed from the front. The medium is composed by rectangular box, which is fed by a conduit at its base. Particles are settled to generate a particle bed having a thickness H_{bed}. Background colors indicate which fluid is present initially in the computational domain. Blue corresponds to the host melt and green to the intruded melt. Red arrows below the conduit represent the velocity profile of the injected fluid (Poiseuille flow). Arrows atop the domain indicate that the boundary condition is a fixed pressure outflow. The hatched walls indicate non-slip boundary conditions. [B] Side view of the computational domain. The green dashed lines indicate that cyclical boundary conditions are used for these walls. The dotted circles indicate particles overlapping with one of the two cyclical boundary conditions and that are also considered to be present on the opposite side. (For interpretation of the colors in the figure(s), the reader is referred to the web version of this article.)

Table 2
Parameters kept constant during the parametric study.

Parameter	Value or range
ρ_p	3300 kg m^{-3}
d_p	4.5-5.5 mm
Nb crystals	208495
H_{bed}	0.3 m
W_{inj}	0.1 m
ρ_i	2500 kg m^{-3}
η_i	1 Pa s
E	2 10^7 Pa
σ	0.32
μ	0.3

ties and viscosities, and injection velocities. The injection velocity and melt viscosity control the stress applied by the input of new materials to the mush. These parameters enter the minimum fluidization velocity, U_{mf} (Schleicher et al., 2016, see supplementary information 2 for derivation of U_{mf}), which expresses the superficial velocity at which the upward drag force equals the reduced weight of the particle bed. This threshold is proportional to the density contrast between the particles and the surrounding melt and inversely proportional to melt viscosity. As the injected melt differs from the host melt, two minimum fluidization velocities can be calculated depending on which melt is considered. For all simulations, we used the minimum of these two velocities, which here always corresponds to that using the host melt properties. The dimensionless injection velocity, U^*, is defined as:

$$U^* = \frac{U_{inj}}{U_{mf}}. \tag{1}$$

In simulations having identical U^*, the injection imposes the same stress to the overlying mush. However, the time needed to inject the same new melt volume changes between simulations because U_{mf} varies. We thus used a dimensionless time, t^*, to scale the simulation time (Bergantz et al., 2017):

$$t^* = \frac{tU_{inj}}{H_{bed}}, \tag{2}$$

where t is the simulation time. In this way, simulations having identical t^* implies that the same volumes of intruder have been injected until that dimensionless time and simulation results can be compared directly. We use the Atwood number to scale the density contrast between the two materials. Here, two Atwood numbers may be defined. The first one, At, expresses the buoyancy contrast between the two melts:

$$At = \frac{\rho_i - \rho_h}{\rho_i + \rho_h}, \tag{3}$$

where ρ_i is the density of the intruded melt, and ρ_h is the host melt density. The second one, At_b, takes the presence of crystals in the host material into account and scales the bulk densities (the weight of material including crystals and melt per unit of volume):

$$At_b = \frac{\rho_i - (\rho_h(1-\Phi) + \rho_p\Phi)}{\rho_i + (\rho_h(1-\Phi) + \rho_p\Phi)}, \tag{4}$$

where Φ is the particle volume fraction. A negative Atwood number indicates that the intruder is buoyant compared to the mush, whereas a positive one indicates a tendency to sink. The viscosity contrast, η^*, between the two melts is expressed as:

$$\eta^* = \frac{\eta_h}{\eta_i}, \tag{5}$$

where η_h is the host dynamic viscosity and η_i is that of the injected melt.

3. Results

We performed 25 numerical simulations to explore the influence of the host melt density and viscosity (see Table 3 for a list of all the simulations and corresponding parameters). For these simulations, the injection velocities are such that the ratio with the respective minimum fluidization velocity, U^*, remains constant at $U^* = 21.2$. This ratio is chosen to match that used previously in similar works (Schleicher et al., 2016; Schleicher and Bergantz, 2017) according to the formula presented in the supplementary material 2. We performed an additional 4 simulations at higher injection velocities to explore the effect of U^* on intrusion dynamics.

Table 3
List of the simulation performed for this study and corresponding variables.

Run nb.	ρ_h (kg m^{-3})	ρ_b (host) (kg m^{-3})	At	At_b	η_h (Pa s)	U_{mf} (m s^{-1})	U_{inj} (m s^{-1})
A1	2500	3012	0	−0,151	1	2.956 10^{-4}	6.268 10^{-3}
A2	2500	3012	0	−0,151	5	5.913 10^{-5}	1.254 10^{-3}
A3	2500	3012	0	−0,151	10	2.957 10^{-5}	6.268 10^{-4}
A4	2500	3012	0	−0,151	50	5.913 10^{-6}	1.254 10^{-4}
A5	2500	3012	0	−0,151	100	2.957 10^{-6}	6.268 10^{-5}
A6	2450	2994	1.0 10^{-2}	−0,146	1	3.141 10^{-4}	6.660 10^{-3}
A7	2450	2994	1.0 10^{-2}	−0,146	5	6.283 10^{-5}	1.332 10^{-3}
A8	2450	2994	1.0 10^{-2}	−0,146	10	3.141 10^{-5}	6.660 10^{-4}
A9	2450	2994	1.0 10^{-2}	−0,146	50	6.283 10^{-6}	1.332 10^{-4}
A10	2450	2994	1.0 10^{-2}	−0,146	100	3.141 10^{-6}	6.660 10^{-5}
A11	2550	3030	−9.9 10^{-3}	−0,155	1	2.772 10^{-4}	5.876 10^{-3}
A12	2550	3030	−9.9 10^{-3}	−0,155	5	5.544 10^{-5}	1.175 10^{-3}
A13	2550	3030	−9.9 10^{-3}	−0,155	10	2.772 10^{-5}	5.876 10^{-4}
A14	2550	3030	−9.9 10^{-3}	−0,155	50	5.544 10^{-6}	1.175 10^{-4}
A15	2550	3030	−9.9 10^{-3}	−0,155	100	2.772 10^{-6}	5.876 10^{-5}
A16	2200	2904	6.4 10^{-2}	−0,123	1	4.065 10^{-4}	8.618 10^{-3}
A17	2200	2904	6.4 10^{-2}	−0,123	5	8.130 10^{-5}	1.724 10^{-3}
A18	2200	2904	6.4 10^{-2}	−0,123	10	4.065 10^{-5}	8.618 10^{-4}
A19	2200	2904	6.4 10^{-2}	−0,123	50	8.130 10^{-6}	1.724 10^{-4}
A20	2200	2904	6.4 10^{-2}	−0,123	100	4.065 10^{-6}	8.618 10^{-5}
A21	2150	2886	7.5 10^{-2}	−0,118	1	4.250 10^{-4}	9.010 10^{-3}
A22	2150	2886	7.5 10^{-2}	−0,118	5	8.500 10^{-4}	1.802 10^{-3}
A23	2150	2886	7.5 10^{-2}	−0,118	10	4.250 10^{-5}	9.010 10^{-4}
A24	2150	2886	7.5 10^{-2}	−0,118	50	8.500 10^{-6}	1.802 10^{-4}
A25	2150	2886	7.5 10^{-2}	−0,118	100	4.250 10^{-6}	9.010 10^{-5}
B1	2150	2886	7.5 10^{-2}	−0,118	100	4.250 10^{-6}	4.250 10^{-3}
B2	2150	2886	7.5 10^{-2}	−0,118	100	4.250 10^{-6}	4.250 10^{-2}
B3	2150	2886	7.5 10^{-2}	−0,118	100	4.250 10^{-6}	4.250 10^{-1}
B4	2150	2886	7.5 10^{-2}	−0,118	100	4.250 10^{-6}	4.250 10^{0}

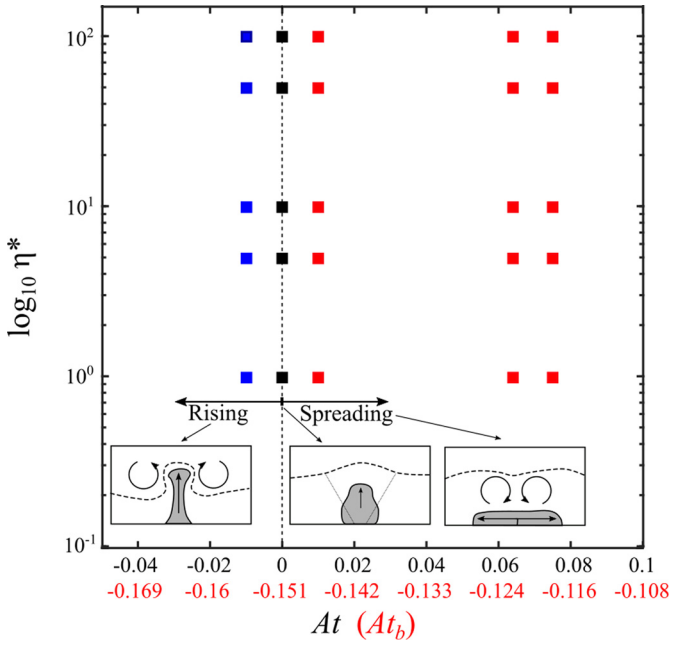

Fig. 2. Regime diagram of intrusion behavior for $U^* = 21.2$. The diagram represents the positions of the simulations A1–25 as functions of the Atwood numbers (abscissa) and viscosity ratios (ordinate). Each square represents a simulation. Square colors depend on the observed regime (blue = rising; black = fluidization; red = lateral spreading). The vertical dashed line interpolates where the fluidization is expected to prevail.

Fig. 2 plots the simulations at the lowest U^*, 21.2, as functions of the dimensionless quantities At, At_b, and η^*. It shows that the intrusions can be classified in three regimes as a function of the Atwood number between the two melts, At. When $\rho_i = \rho_h$, the *fluidization* regime is observed. If $\rho_i > \rho_h$, the *spreading* regime occurs, whereas if $\rho_i < \rho_h$, the *rising* regime occurs (see next paragraph for a detailed description of the regime dynamics). The bulk Atwood number At_b is always negative and the regime transition occurs at a value (−0.151) of no particular physical significance. The three regimes do no depend on the viscosity contrast η^*.

The *fluidization* regime was observed in the simulations once $\rho_i = \rho_h$, and consists in the development of a fluidized area above the inlet in which the intruded melt rises through the mush (Fig. 3A–C), as described previously (Bergantz et al., 2015; Schleicher et al., 2016). The fluidization of the mush is initiated by the dilation of the crystal framework to crystal volume fraction below 0.3 above the inlet that locally destabilizes the forces chains network that supports the bed and separates the crystals in contact. The fluidized volume grows vertically above the inlet because of two mechanisms. The first is the upward entrainment of the particles localized above the fluidized cavity, which results in bulging the top surface of the mush layer (Fig. 3A–C). The second mechanism is the progressive erosion of the crystals jammed at the boundary between the mush and the fluidized volume. Once separated, crystals start settling in the fluidized area because of this process of mush erosion, causing the fluidized area to ascend faster than the intruded melt (green outline in Fig. 3A–C). The intruder flows mainly vertically with a minor lateral porous flow. When the fluidized cavity reaches the top of the particle bed, its width progressively decreases to stabilize in the shape of a vertical chimney. At steady state, when $t^* > 1$, the crystals located within the chimney show both upward and downward motions whereas the ones located around the chimney flow slowly in the direction of the inlet, forming a 'mixing bowl' as a whole, fully recovering the dynamics first described in Bergantz et al. (2015).

The *spreading* regime, which prevails in simulations once $\rho_i > \rho_h$, is characterized by the lateral spreading of the injected melt similarly to a gravity current hugging the floor of the host reservoir (Fig. 3D–F). The main difference with a pure fluid gravity current is that the melt is progressively flowing across the mush as permeable flow. At the start of the injection, the crystal framework experienced a dilation, which initiates host crystals settling in the

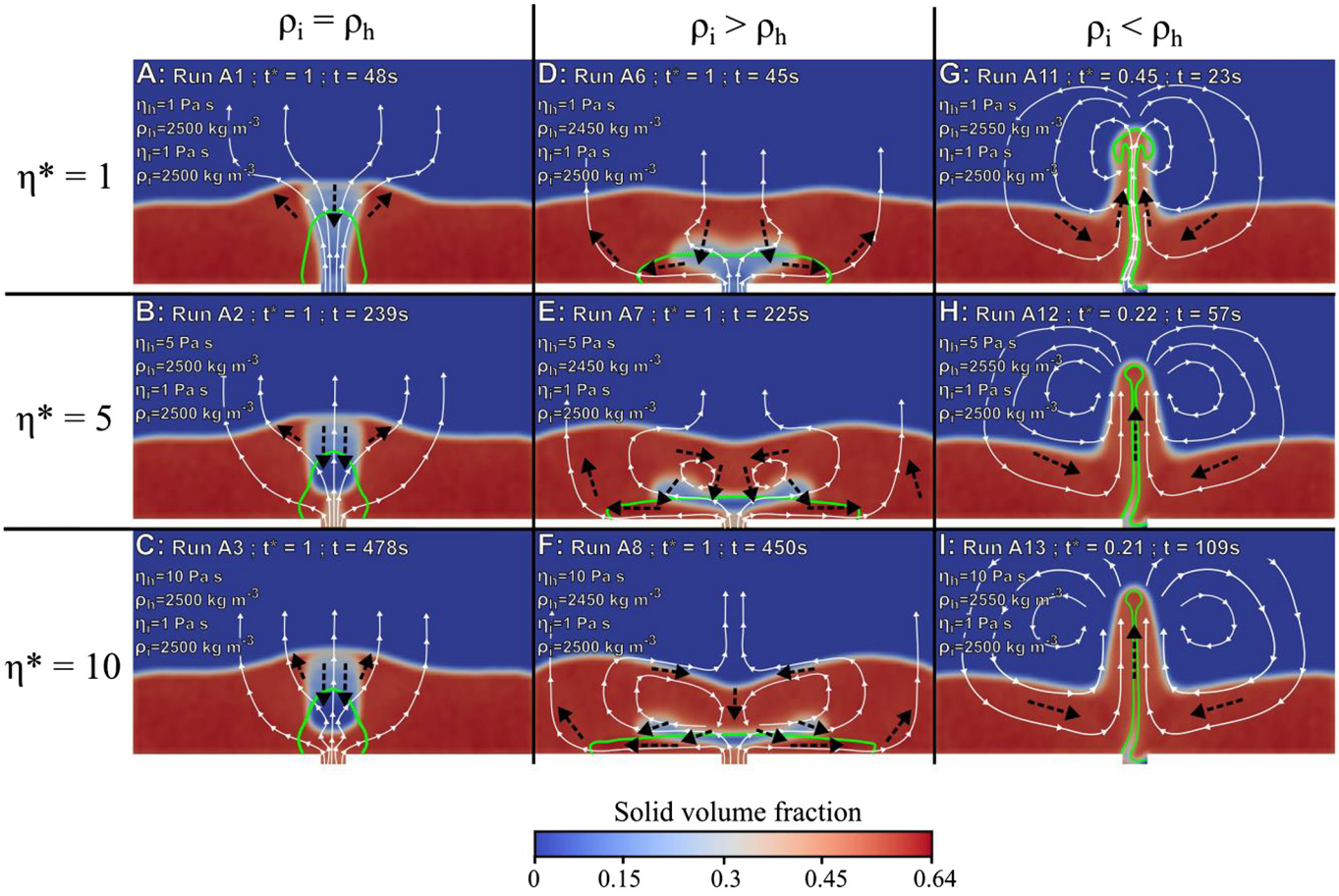

Fig. 3. Comparison of the effects of buoyancy and viscosity contrasts. Each section represents the advancement of the simulation at $t^* = 1$ (or when the rising instability is above the particle bed). The injected melt contours are indicated with green curves. The dashed black arrows indicate the presence and direction of granular flows. The thin white curves indicate the fluid streamlines with small arrowheads indicating flow direction.

same fashion as in the *fluidization* regime. The lateral flow of the intruded melt is able to laterally entrain the host crystals, creating two counter rotating granular vortexes in the residing mush with downward motions above the inlet (Fig. 3D–F). Such granular vorticity affects the flow pattern of the fluid in the mush. The fluidized volume grows either predominantly laterally or vertically, depending on the relative importance between the lateral entrainment of the host solids by the intruder and the vertical settling of the mush crystals. As the lateral propagation of the intruder progresses, so does the size of the two granular vortexes, making this style of intrusion affect a larger mush volume than the *fluidization* regime.

The *rising* regime (Fig. 3G–I), is characterized by the ascent of the intruded melt within the mush that occurred in simulations once $\rho_i < \rho_h$. Runs start with the initial growth above the inlet of a cavity filled with the intruded fluid. The cavity becomes gravitationally unstable and ascends within the mush, forming a Rayleigh-Taylor instability. The ascent of the intruder continues above the particle bed, entraining solids from the host. The instability is driven by its head because of the buoyant batch of intruded melt. This driving batch is surrounded by a volume of fluidized host mush (Fig. 3G–I, better seen in Supplementary Movie 3 as the absence of particle overlap). The dimensionless time at which the intrusion reaches the mush top ($t^* \sim 0.3$) is shorter than that of the two other regimes because the Rayleigh-Taylor instability significantly accelerates the transport of the intruder.

Fig. 2 suggests that the viscosity contrast does not control the end-member shape of the intruder flow. Larger viscosity contrasts, however, increase the trends of some aspects of mush dynamics. Fig. 3 illustrates how viscosity bears on flow patterns.

In the *fluidization* regime, the increase of the host viscosity enhances the formation of crystal-poor batches at the top of the intruded volume (Fig. 3A–C). Because the minimum fluidization velocity within the intruded melt is higher than for the host, the crystals are not fluidized and sediment in the intruded melt to accumulate atop the inlet (Fig. 3B–C). Because we defined t^* to scale the dynamics of the mush, the increase of the host melt viscosity decreases the injection velocity and increases the duration, t, required to reach the dimensionless time $t^* = 1$. As a result, increasing melt viscosity decreases the ability for the intruded melt to experience lateral porous flow through the host crystal frameworks (Fig. 3B–C). It also increases the ratio between crystal terminal velocity in the intruded and host melts, which results in the formation of the crystal poor volume at the top of the intruded volume (Fig. 3B–C). The increase in the host melt viscosity, however, does not affect the volume of mush inflated by the injection and showing distortion of the force chains.

In the *spreading* regime, high viscosity contrasts enhance the lateral spreading of the intruder and the entrainment of the host crystals in the two counter rotating vortexes (Fig. 3E–F). Large host melt viscosity causes the lateral entrainment of the solids to be more efficient than particle settling, which results in the elongation of the fluidized volume in the horizontal direction. In the same fashion as in the *fluidization* regime, the lower superficial injection rate diminishes the ability of the lateral flow to entrain particles, which increases the number of host crystals present in the intruded layer. This effect is expressed by the decrease of the

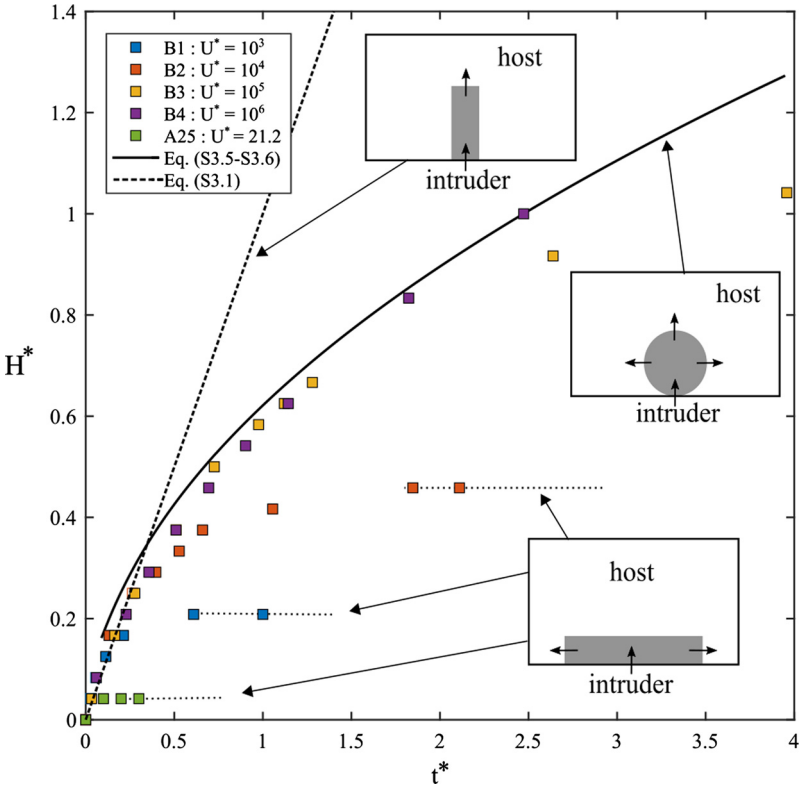

Fig. 4. Evolution of the height, H^*, of the intruded volume as a function of the dimensionless time t^*. Each square represents the height of the top of the intruded volume measured in the simulations. Square colors indicate injection rate. Dashed lines indicate the theoretical intruder front height evolution in the case of vertical propagation (supplementary information 3) The black curve is the theoretical front height for a radial growth, and the horizontal dotted lines indicate the front height evolution during lateral spreading. The three insets illustrate intrusion behaviors.

thickness of the intruded layer with the increase of the host viscosity (Fig. 3D–F). It results that reaching the same volume of mush entrained by the intrusion requires less intruded material as the viscosity of the host melt increases.

In the *rising* regime, increasing the viscosity contrast enlarges the vortexes sizes and the separation distance between their centers (Fig. 3G–I). The dimensionless time, t^*, at which the intruder instability occurs decreases with the viscosity of the host. The volume of the intruded melt driving the Rayleigh-Taylor instabilities is lower when a viscosity contrast exists. When a viscosity contrast is present, the volume of the intruded melt driving the instability does not vary significantly (Fig. 3H–I). The greater thickness of the intruder when the Rayleigh-Taylor instability significantly accelerates can be explained by considering the ratio between the dimensional injection rate and Rayleigh-Taylor growth rate. In Fig. 3G, this ratio is higher than in Fig. 3H–I, and a significant volume of fluid is injected before the instability accelerates. On the contrary, in Fig. 3H–I, this ratio is small and so is the amount of melt injected before the acceleration of the instability. However, the volume of the mush remobilized by the intruder flow does not significantly vary with the host melt viscosity (Fig. 3G–I).

The additional 4 simulations in the spreading regime suggest that buoyancy effects dominate the intruder flow up to U^* 10^5. Fig. 4 shows the temporal evolution of the dimensionless height reached by the intruded volume, H^* ($H^* = H/H_{bed}$, where H is the maximum height of the intrusion), as a function of injection rate. All injections grow purely vertically at first ($t^* \leq 0.1$). As seen above, at the low injection rate of 21.2, the intrusion stalls rapidly and spreads laterally (simulation A25, Fig. 4). Increasing the injection rate causes stalling to occur later and higher. When $t^* > 0.2$, injection growth switches from vertical to radial. When $U^* > 10^5$, the behavior of the intruder is dominated by the injection rate, which causes the radially growing intrusion to reach the top of the bed at $H^* = 1$. Despite that all simulations have the same intruder shape before stalling, the size of the region surrounding the intruder that is affected by dilatancy increases with U^*. The highest injection rate (simulation B4 with $U^* = 10^6$) strictly follows the theoretical curve for a radial growth and reaches $H^* = 1$ at $t^* \approx 2.5$, as predicted by geometrical arguments (supplementary information 3).

Mush dilation is key for permeable melt flow to occur. The initiation of the intrusion increases the pore pressure in the mush around the inlet (Fig. 5A). This overpressure progressively propagates outwards and decreases the crystal volume fraction in the overlying mush (Fig. 5B). As the intrusion propagates, the effect of the overpressure is supplemented with the Reynolds dilatancy generated by the granular vortexes in the mush (Fig. 5C). The dilation of the solid framework increases its permeability and in turn the possibility of relative motion between the crystals and the interstitial melt (Fig. 5C). This phenomenon is particularly clear in the case of the rising regime. The intruder is surrounded by a volume of mush that underwent such dilation that it is in the dilute regime. The contact region between the two magmas is dominated by melt–melt interface interspersed with isolated crystals. As a result, entrainment is ruled by melt vorticity.

4. Comparison with natural systems

To test the applicability of our results to natural cases, we gathered from the literature the physical parameters of 13 eruptions involving the intrusion of new magma (Table S3–S4 in the supplementary information 5). All host magmas are well-characterized but for a few cases for which there is ambiguity on the respective roles of the intruder and host magmas (Unzen, Minoan, and Katmai–Novarupta). In the studies surveyed, melt viscosity and melt density of host magmas were most often directly determined

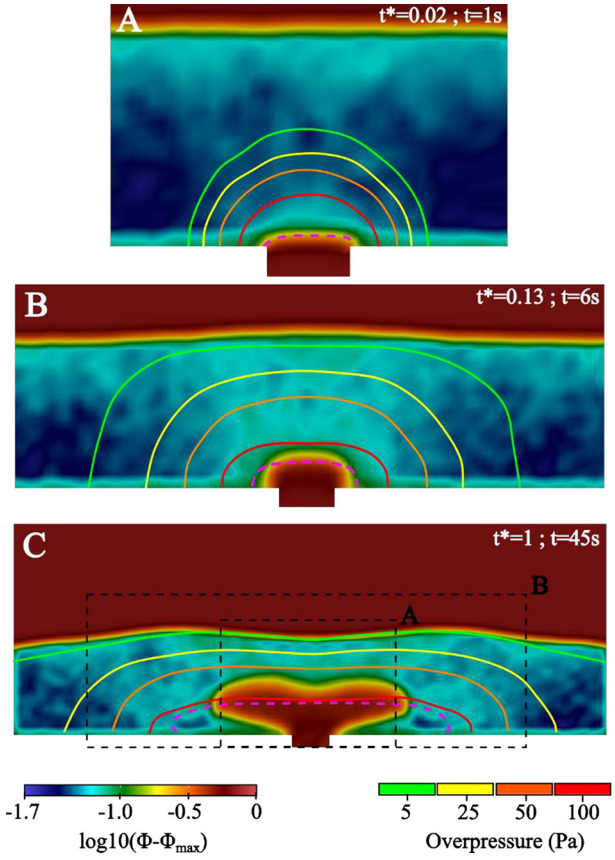

Fig. 5. Evolution of the pore pressure and crystal volume fraction. On each inset, the color depend on the difference between the local crystal volume fraction, Φ, and the maximum one, Φ_{max} ($\Phi_{max} = 0.64$), in a logarithmic scale. The overpressure with respect to the initial hydrostatic pressure field is indicated with contour that corresponds to the isosurfaces where the overpressure are equal to 5, 25, 50, and 100 Pa. The pink dashed curves represent the boundary between the injected and resident melt. Inset [A] and [B] are captured after 1 s and 6 s. Both only displayed the portion of the mush layer that present overpressure and dilation. Inset [C] is acquired after 45 s and cover a slice of the entire computational domain. The two dashed rectangle indicate the extent of insets [A] and [B].

from eruptive products and pre-eruptive conditions such as pressure, temperature, and melt water content (details on how parameters were obtained are in Table S3–S4 (see supplementary information 5)).

Cases are organized into three categories depending on the observed eruptive sequence. In the first category, the intruder was erupted first, followed by the emission of host magma or a mixture of host and intruder. This category implies that the intruder magma was able to efficiently penetrate and pass through the host magma. In the second category, both host and intruder magmas were erupted simultaneously, with the intruder most often forming enclaves or mingling structures. The last category feature cases where the mixing was so thorough that the eruptive products only bear cryptic traces of the intruder, such as isolated intruder crystals floating in the host or crystal disequilibrium textures.

Fig. 6A shows the ratios of bulk viscosities and bulk densities between the intruder magma and the host magma(s) for the 13 eruptions. Fig. 6A contains two physically meaningful thresholds, that of neutral buoyancy at the bulk density ratio of 0 and that of equal viscosity at the bulk viscosity ratio of one. The three types of eruptive sequence are not sorted following any of these thresholds. Fig. 6B shows the same eruptions plotted as functions of melt properties instead of bulk properties. Our numerical runs cover the full range of natural density ratios and a more restricted range of viscosity ratios (from 1 to 10^2 vs. 10^{-2} to 10^4 in nature). Fig. 6B also shows the dividing line between rising and spreading dynamics at the level of neutral buoyancy with respect to the melts. With the possible exception of the 1912 Katmai–Novarupta eruption (see *Discussion*), the *rising* regime is populated by the eruptions that first ejected intruder material. This divide between cases where at least some of the intruder magma had the capacity to go unscathed through the host and cases where none of it escaped from host interaction is consistent with our numerical results.

5. Discussion

Our results are helpful to predict the behavior of an intrusion within a mush. The Atwood number between the two melts, *At*, is the parameter having a first order control on the geometry of the intrusion. On the contrary, the commonly used level of neutral bulk buoyancy (e.g. Huppert et al., 1986; Snyder and Tait, 1995) does not mark any particular change in dynamic behavior (Fig. 2). This result illustrates that the relative motion between the solids and surrounding melt is of primary importance when studying mush processes. Experiments, or numerical simulations, that account of the presence of the solids or exsolved volatiles as discrete entities (e.g. Barth et al., 2019; Bergantz et al., 2015; Burgisser et al., 2020; Carrara et al., 2019; Girard and Stix, 2009; Hodge et al., 2012; McIntire et al., 2019; Michioka and Sumita, 2005; Parmigiani et al., 2014; Schleicher et al., 2016; Schleicher and Bergantz, 2017) are the most likely to faithfully reproduce mush dynamics. Neglecting phase decoupling by considering the magma as a single-phase fluid having effective properties such as bulk density or bulk viscosity will not capture the blending of crystal contents between host and intruder and the simultaneous but independent evolution of the melt–melt interface (Fig. 5C).

The decoupling between the motions of the two phases results from processes unique to granular mechanics that our discrete numerical model is able to capture. Mush dilation causes entrainment by melt vorticity alone (Fig. 5). Efficient entrainment of two fluids with a viscosity contrast occurs only when the most viscous fluid bears large levels of vorticity (Jellinek and Kerr, 1999). In our runs, the intruder melt viscosity is equal or less than that of the host, and the vorticity is concentrated close to or inside the intrusion (Fig. S4 in the supplementary information 4). This situation yields the weak entrainment observed in the rising regime and the transition from vertical growth to spreading of the intrusion melt as injection velocity decreases (Fig. 4). The concept of bulk density thus fails to predict the intrusion geometry for two reasons. First, it assumes the absence of relative motion and thus ignores the transfer of crystals from host to intrusion. Second, in cases when sufficient mush dilation occurs, entrainment is controlled by the melt–melt interface and the associated density and viscosity contrasts. The interplay between pore pressure, dilation, melt interface dynamics, and permeable flow controls the transport of mass within our modeled magmatic reservoir.

We characterized the parameter ranges of a series of well-documented cases of eruptions that features magma mixing, focusing on the densities and viscosities of the two end-member magmas involved and on the order of the eruptive sequence. One case, Katmai, straddles two eruptive sequence categories because the intruders may have been transported alongside (as opposed to through) the host magmas. Both scenarios are close to the neutral buoyancy level (Fig. 6B) and each individual scenario is consistent with our regimes. The Katmai eruption first emitted rhyolite. The Katmai scenario corresponding to a rhyolite intruding a more mafic host (Eichelberger and Izbekov, 2000) is consistent with it being located in the *rising* regime. In the other scenario (Singer et al., 2016), the rhyolite is part of the host reservoir, which is consistent with that scenario being in the spreading regime. The overall good agreement between the observed eruptive sequences and our nu-

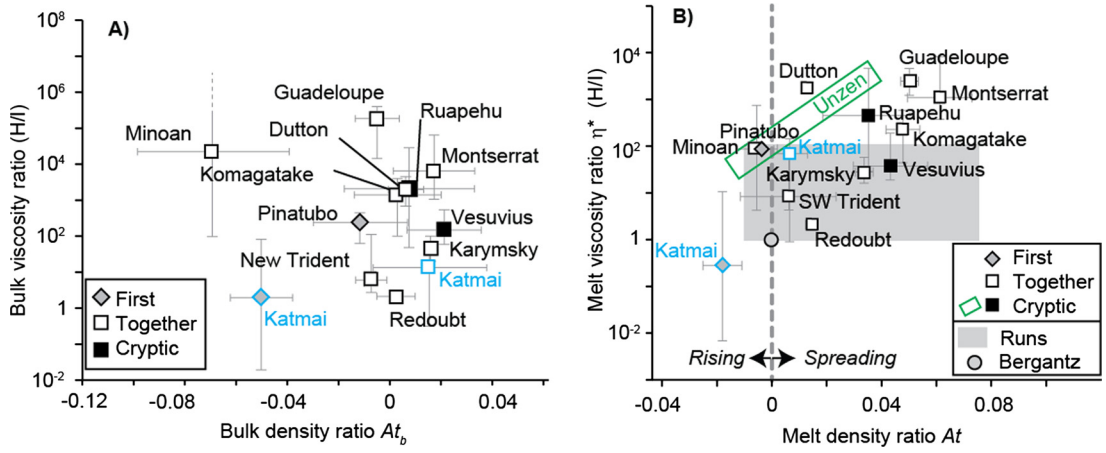

Fig. 6. Ratios of physical properties for the host and intruder magmas involved in 13 eruptions. Viscosity ratios are that of the host over that of the intruder and the density ratios are measured by the Atwood numbers. Eruptions are sorted according to whether the intruder magma was erupted first ("First"), at the same time as (or mixed with) the host ("Together"), or fully mixed with the host ("Cryptic"). [A] Ratios of bulk properties. [B] Ratios of melt properties. The gray area covers the runs done in this study and the circle marks the parameters used in the numerical study of Bergantz et al. (2015). See text for details regarding the special case of Unzen.

merical results (Fig. 6B) supports the fact that open-system events are, to first order, controlled by the density contrast between the melt phases of the intrusion and mush. It also suggests that injection momentum was quickly exhausted, letting buoyancy control the unfolding of the event.

One special natural case can be evaluated against our dynamic regimes. The intruder of the 1991–1995 eruption of Unzen volcano could have been either andesitic (Holtz et al., 2005), or basaltic (Browne et al., 2006). Regardless of its composition, the intrusion caused thorough mixing and the first magma erupted was the product of this mixing. If the intruder was basaltic, it was buoyant with respect to the felsic host and if it was andesitic, it was denser that the host. As a result, Unzen spans the divide between the *rising* and *spreading* regime (Fig. 6B). Considering that the intruder input was large (>30 wt% of the eruptive products; Holtz et al., 2005), and if any credit is given to our inferences, the intruder was more likely to be andesitic than basaltic because this latter composition would have been prone to preserve its integrity while going through the host mush, erupting first.

6. Conclusions

This study highlights the importance of granular mechanics in mush processes, which differ significantly from ones expected with purely fluid models. As expected, our simulations show that when the injection velocity is high ($U^* > 10^5$), intrusion dynamics is dominated by the injection momentum and the intruded cavities grow radially. When the injection velocity is below this threshold, however, buoyancy controls the behavior of the intruder in an unexpected way. Bulk buoyancy contrasts appear to play no role in the way the intruder flows. Instead, the density contrast between the host and intruded melts exerts a first-order control on the architecture of an intrusion event in a mush. When the two melt densities are identical, the intruder fluidizes the mush and creates a mixing bowl, as described in Bergantz et al. (2015). When the intruded melt is lighter than that of the host, it rises through the mush. Mush dilation around the intruder causes the contact region between the two magmas to be dominated by melt–melt interface interspersed with isolated crystals. Entrainment in this rising regime is ruled by the amount of vorticity of the most viscous melt. As in our runs the intruder melt viscosity was equal or lower than that of the host, no entrainment was observed. Intruder melts denser than the host spread laterally partly as permeable flows through the host mush. The lateral spreading of the intruder generates two counter rotating granular vortexes with downward motions above the inlet, which maximizes the volume of the mush entrained by the gravity current. In this spreading regime, the combined effects of the initial pore overpressure at the inlet and the Reynolds dilatancy resulting from the lateral spreading of the intruder are able to fluidize the overlying mush.

We tested whether the first-order effect of melt density contrast was expressed in nature. We tallied 13 well-documented eruptive sequences, classifying them according to the expected outcomes of the three dynamic regimes we defined. We found overall good agreement between eruption sequences and our model predictions, which suggests that pore pressure, dilatancy, and permeable flow play a fundamental role in the unfolding of open-system events. Granular dynamics and the decoupling of melt and crystals are thus key in shaping reservoir and volcanic processes.

CRediT authorship contribution statement

Alexandre Carrara: Conceptualization, Methodology, Software, Investigation, Writing - review & editing. **Alain Burgisser:** Conceptualization, Investigation, Writing - review & editing. **George W. Bergantz:** Conceptualization, Writing - review & editing.

Declaration of competing interest

Authors declare no conflicts of interest.

Acknowledgements

All the numerical simulations presented in this paper were performed using the CIMENT infrastructure (https://ciment.ujf-grenoble.fr), which is supported by the Rhône-Alpes region (GRANT CPER07_13 CIRA: http://www.ci-ra.org). Author thanks C.P. Montagna and C. Huber for their helpful reviews and comments that significantly improved this manuscript, and H. Handley for her editorial handling. This work was partially supported by the Agence Nationale pour la Recherche grant ANR-19-CE31-0007. G.W.B. was supported by National Science Foundation grants DGE-1256068, EAR-1049884 and EAR-1447266.

Appendix A. Supplementary material

Supplementary material related to this article can be found online at https://doi.org/10.1016/j.epsl.2020.116539.

References

Annen, C., Blundy, J.D., Leuthold, J., Sparks, R.S.J., 2015. Construction and evolution of igneous bodies: towards an integrated perspective of crustal magmatism. Lithos 230, 206–221. https://doi.org/10.1016/j.lithos.2015.05.008.

Annen, C., Blundy, J.D., Sparks, R.S.J., 2006. The genesis of intermediate and silicic magmas in deep crustal hot zones. J. Petrol. 47, 505–539. https://doi.org/10.1093/petrology/egi084.

Bachmann, O., Bergantz, G.W., 2006. Gas percolation in upper-crustal silicic crystal mushes as a mechanism for upward heat advection and rejuvenation of near-solidus magma bodies. J. Volcanol. Geotherm. Res. 149, 85–102. https://doi.org/10.1016/j.jvolgeores.2005.06.002.

Bachmann, O., Huber, C., 2016. Silicic magma reservoirs in the Earth's crust. Am. Mineral. 101, 2377–2404. https://doi.org/10.2138/am-2016-5675.

Barth, A., Edmonds, M., Woods, A., 2019. Valve-like dynamics of gas flow through a packed crystal mush and cyclic strombolian explosions. Sci. Rep. 9, 1–9. https://doi.org/10.1038/s41598-018-37013-8.

Bergantz, G.W., 1989. Underplating and partial melting: implications for melt generation and extraction. Science 245, 1093–1095. https://doi.org/10.1126/science.245.4922.1093.

Bergantz, G.W., Breidenthal, R.E., 2001. Non-stationary entrainment and tunneling eruptions: a dynamic link between eruption processes and magma mixing. Geophys. Res. Lett. 28, 3075–3078. https://doi.org/10.1029/2001GL013304.

Bergantz, G.W., Schleicher, J.M., Burgisser, A., 2015. Open-system dynamics and mixing in magma mushes. Nat. Geosci. 8, 793–796. https://doi.org/10.1038/ngeo2534.

Bergantz, G.W., Schleicher, J.M., Burgisser, A., 2017. On the kinematics and dynamics of crystal-rich systems. J. Geophys. Res., Solid Earth 122, 2017JB014218. https://doi.org/10.1002/2017JB014218.

Browne, B.L., Eichelberger, J.C., Patino, L.C., Vogel, T.A., Uto, K., Hoshizumi, H., 2006. Magma mingling as indicated by texture and Sr/Ba ratios of plagioclase phenocrysts from Unzen volcano, SW Japan. In: Modern Trends in Petrography. J. Volcanol. Geotherm. Res. 154, 103–116. https://doi.org/10.1016/j.jvolgeores.2005.09.022.

Burgisser, A., Bergantz, G.W., 2011. A rapid mechanism to remobilize and homogenize highly crystalline magma bodies. Nature 471, 212–215. https://doi.org/10.1038/nature09799.

Burgisser, A., Carrara, A., Annen, C., 2020. Numerical simulations of magmatic enclave deformation. J. Volcanol. Geotherm. Res. 392, 106790.

Caricchi, L., Annen, C., Blundy, J., Simpson, G., Pinel, V., 2014. Frequency and magnitude of volcanic eruptions controlled by magma injection and buoyancy. Nat. Geosci. 7, 126–130. https://doi.org/10.1038/ngeo2041.

Carrara, A., Burgisser, A., Bergantz, G.W., 2019. Lubrication effects on magmatic mush dynamics. J. Volcanol. Geotherm. Res. 380, 19–30.

Cashman, K.V., Sparks, R.S.J., Blundy, J.D., 2017. Vertically extensive and unstable magmatic systems: a unified view of igneous processes. Science 355, eaag3055. https://doi.org/10.1126/science.aag3055.

Couch, S., Sparks, R.S.J., Carroll, M.R., 2001. Mineral disequilibrium in lavas explained by convective self-mixing in open magma chambers. Nature 411, 1037–1039. https://doi.org/10.1038/35082540.

Dufek, J., Bergantz, G.W., 2005. Lower crustal magma genesis and preservation: a stochastic framework for the evaluation of basalt–crust interaction. J. Petrol. 46, 2167–2195. https://doi.org/10.1093/petrology/egi049.

Eichelberger, J.C., Izbekov, P.E., 2000. Eruption of andesite triggered by dyke injection: contrasting cases at Karymsky Volcano, Kamchatka and Mt Katmai, Alaska. Philos. Trans. R. Soc. A, Math. Phys. Eng. Sci. 358, 1465–1485.

Garg, R., Galvin, J., Li, T., Pannala, S., 2012. Open-source MFIX-DEM software for gas–solids flows: part I—verification studies. Powder Technol. 220, 122–137.

Girard, G., Stix, J., 2009. Buoyant replenishment in silicic magma reservoirs: experimental approach and implications for magma dynamics, crystal mush remobilization, and eruption. J. Geophys. Res. 114, B08203. https://doi.org/10.1029/2008JB005791.

Hodge, K.F., Carazzo, G., Jellinek, A.M., 2012. Experimental constraints on the deformation and breakup of injected magma. Earth Planet. Sci. Lett. 325–326, 52–62. https://doi.org/10.1016/j.epsl.2012.01.031.

Holtz, F., Sato, H., Lewis, J., Behrens, H., Nakada, S., 2005. Experimental petrology of the 1991–1995 Unzen dacite, Japan. Part I. Phase relations, phase composition and pre-eruptive conditions. J. Petrol. 46, 319–337.

Huber, C., Bachmann, O., Dufek, J., 2011. Thermo-mechanical reactivation of locked crystal mushes: melting-induced internal fracturing and assimilation processes in magmas. Earth Planet. Sci. Lett. 304, 443–454. https://doi.org/10.1016/j.epsl.2011.02.022.

Huppert, H.E., Sparks, R.S.J., Whitehead, J.A., Hallworth, M.A., 1986. Replenishment of magma chambers by light inputs. J. Geophys. Res., Solid Earth, 6113–6122. https://doi.org/10.1029/JB091iB06p06113@10.1002/(ISSN)2169-9356.OPENSYS1.

Jellinek, A.M., Kerr, R.C., 1999. Mixing and compositional stratification produced by natural convection: 2. Applications to the differentiation of basaltic and silicic magma chambers and komatiite lava flows. J. Geophys. Res., Solid Earth 104, 7203–7218. https://doi.org/10.1029/1998JB900117.

Karakas, O., Degruyter, W., Bachmann, O., Dufek, J., 2017. Lifetime and size of shallow magma bodies controlled by crustal-scale magmatism. Nat. Geosci. 10, 446–450. https://doi.org/10.1038/ngeo2959.

Koyaguchi, T., Kaneko, K., 2000. Thermal evolution of silicic magma chambers after basalt replenishments. Earth Environ. Sci. Trans. R. Soc. Edinb. 91, 47–60. https://doi.org/10.1017/S0263593300007288.

Li, T., Garg, R., Galvin, J., Pannala, S., 2012. Open-source MFIX-DEM software for gas-solids flows: part II—validation studies. Powder Technol. 220, 138–150.

McIntire, M.Z., Bergantz George, W., Schleicher, Jillian M., 2019. On the hydrodynamics of crystal clustering. Philos. Trans. R. Soc. A, Math. Phys. Eng. Sci. 377, 20180015. https://doi.org/10.1098/rsta.2018.0015.

Michioka, H., Sumita, I., 2005. Rayleigh-Taylor instability of a particle packed viscous fluid: implications for a solidifying magma. Geophys. Res. Lett. 32. https://doi.org/10.1029/2004GL021827.

Parmigiani, A., Huber, C., Bachmann, O., 2014. Mush microphysics and the reactivation of crystal-rich magma reservoirs. J. Geophys. Res., Solid Earth 119, 6308–6322. https://doi.org/10.1002/2014JB011124.

Schleicher, J.M., Bergantz, G.W., 2017. The mechanics and temporal evolution of an open-system magmatic intrusion into a crystal-rich magma. J. Petrol. 58, 1059–1072. https://doi.org/10.1093/petrology/egx045.

Schleicher, J.M., Bergantz, G.W., Breidenthal, R.E., Burgisser, A., 2016. Time scales of crystal mixing in magma mushes. Geophys. Res. Lett. 43, 1543–1550. https://doi.org/10.1002/2015GL067372.

Singer, B.S., Costa, F., Herrin, J.S., Hildreth, W., Fierstein, J., 2016. The timing of compositionally-zoned magma reservoirs and mafic 'priming' weeks before the 1912 Novarupta-Katmai rhyolite eruption. Earth Planet. Sci. Lett. 451, 125–137. https://doi.org/10.1016/j.epsl.2016.07.015.

Snyder, D., Tait, S., 1995. Replenishment of magma chambers: comparison of fluid-mechanic experiments with field relations. Contrib. Mineral. Petrol. 122, 230–240. https://doi.org/10.1007/s004100050123.

Syamlal, M., 1998. MFIX Documentation Numerical Technique. EG and G Technical Services of West Virginia, Inc., Morgantown, WV (United States).

Syamlal, M., Rogers, W., O'Brien, T.J., 1993. MFIX Documentation Theory Guide. USDOE Morgantown Energy Technology Center, WV (United States).

Weinberg, R.F., Leitch, A.M., 1998. Mingling in mafic magma chambers replenished by light felsic inputs: fluid dynamical experiments. Earth Planet. Sci. Lett. 157, 41–56. https://doi.org/10.1016/S0012-821X(98)00025-9.

Wiebe, R.A., 2016. Mafic replenishments into floored silicic magma chambers. Am. Mineral. 101, 297–310. https://doi.org/10.2138/am-2016-5429.

Supplementary Information 1:

This supplementary material presents an overview of the numerical model (Garg et al, 2012; Syamlal, 1998; Syamlal et al. 1993). After presenting the method of solution, we compare the magmas physical properties used in the simulations against the range expected in natural magmatic reservoirs. We next validate the ability of the numerical model to model the flow and possible mixing between two miscible fluids and discuss validity limits. Finally, the last part lists the equations used in the numerical model.

S1.A Overview of the numerical model

For the two miscible fluid phases, the equation system comprises the mass and momentum conservations. We used two constitutive equations to link the local melt density and viscosity as a function of the local composition in host and injected fluids. The mass conservation for an uncompressible fluid in a multiphase flow is (Ishii and Hibiki, 2011):

$$\frac{\partial(1-\Phi)}{\partial t}+\nabla\cdot\left((1-\Phi)\boldsymbol{u}\right)=0, \tag{S1.1}$$

where Φ is the solid volume fraction, and $\boldsymbol{u}$ is the fluid velocity vector. The momentum conservation is:

$$\rho_f\frac{D(1-\Phi)\boldsymbol{u}}{Dt}=-\nabla\cdot\left((1-\Phi)P\right)+\nabla\cdot\underline{\underline{\boldsymbol{\sigma}_v}}+(1-\Phi)\rho_f\boldsymbol{g}+I_{fs}, \tag{S1.2}$$

where ρ_f is the fluid density, P is the pressure, $\underline{\underline{\boldsymbol{\sigma}_v}}$ is the fluid viscous stress tensor, $\boldsymbol{g}$ is the gravitational acceleration vector, D/Dt is the material derivative operator, and $\boldsymbol{I_{fs}}$ is the fluid-solid momentum exchange vector. The fluid stress tensor is:

$$\underline{\underline{\boldsymbol{\sigma}_v}}=2\eta(1-\Phi)\underline{\underline{\boldsymbol{\epsilon}_f}}-\frac{2}{3}\eta(1-\Phi)tr\left(\underline{\underline{\boldsymbol{\epsilon}_f}}\right)\underline{\underline{\boldsymbol{\delta}_{ij}}}. \tag{S1.3}$$

where $\boldsymbol{\eta}$ is the dynamic viscosity of the fluid, $\underline{\underline{\boldsymbol{\delta}_{ij}}}$ is the Kronecker delta, and $\underline{\underline{\boldsymbol{\epsilon}_f}}$ is the fluid strain rate tensor computed as:

$$\underline{\underline{\boldsymbol{\epsilon}_f}}=\frac{1}{2}\left(\nabla\boldsymbol{u}+(\nabla\boldsymbol{u})^T\right). \tag{S1.4}$$

As we have two fluids having distinct densities and viscosities in our simulations, the local melt density and viscosity is computed as function of the local concentration in host, C_h, and injected, C_i, fluids as:

$$C_h+C_i=1 \tag{S1.5}$$

$$\eta=\eta_h C_h+\eta_i C_i \tag{S1.6}$$

$$\rho_f=\rho_h C_h+\rho_i C_i \tag{S1.7}$$

The transport equation of the concentration in host and intruded fluids is:

$$\frac{\partial C_i}{\partial t} - \boldsymbol{u} \cdot \nabla C_i = 0 \qquad \text{(S1.8)}$$

Crystal motions were computed by solving the Newton's second laws of motions. Translational motions are governed by:

$$m \frac{d v}{dt} = \sum \boldsymbol{F}_C + \boldsymbol{F}_{fs} + m \boldsymbol{g}, \qquad \text{(S1.9)}$$

where, $\boldsymbol{v}$ is the crystal velocity vector, $\boldsymbol{F}_c$ represents the contact force vector, $\boldsymbol{F}_{fs}$ is the momentum exchange force, and m is the crystal mass. The sum on the right-hand side expresses the summation over all the particles in contact with the particle traveling at $\boldsymbol{v}$. Rotational motion are given by:

$$I \frac{d \boldsymbol{\omega}}{dt} = \sum \boldsymbol{T}_C, \qquad \text{(S1.10)}$$

where I is the crystal moment of inertia, $\boldsymbol{\omega}$ is the crystal rotation vector, and $\boldsymbol{T}_c$ represents the contact torque.

Contacts are modeled with a soft sphere approach (Tsuji et al., 1993), which is a spring-dashpot model, meaning that only a part of the energy is conserved whereas the rest is dissipated during a contact. The total contact force between two crystals may be split in normal (collision), $\boldsymbol{F}_C^{\,n}$, and tangential (friction) components, $\boldsymbol{F}_C^{\,t}$. The total collisional force, $\boldsymbol{F}_C$, is then expressed as:

$$\boldsymbol{F}_C = \boldsymbol{F}_C^{\,n} + \boldsymbol{F}_C^{\,t}. \qquad \text{(S1.11)}$$

The collisional torque involves the distance between each particle center of mass and contact point, L:

$$\boldsymbol{T}_C = L \boldsymbol{\eta}_c \wedge \boldsymbol{F}_C^{\,t}, \qquad \text{(S1.12)}$$

where $\boldsymbol{\eta}_c$ is the unit vector between the centers of mass of the two crystals in contact.

The normal contact force between two particles is expressed as:

$$\boldsymbol{F}_C^{\,n} = \boldsymbol{F}^{\boldsymbol{n}}_S + \boldsymbol{F}^{\boldsymbol{n}}_D. \qquad \text{(S1.13)}$$

The first term on the right hand side of Eq. S1.13 is the conservative part of the contact force (spring), $\boldsymbol{F}^{\boldsymbol{n}}_S$, and the second one the dissipative part (dashpot), $\boldsymbol{F}^{\boldsymbol{n}}_D$. The conservative part is a function of the overlap distance between the two particles, δ_n, and of the spring coefficient, k_n:

$$\boldsymbol{F}^{\boldsymbol{n}}_S = -k_n \delta_n \boldsymbol{\eta}_c, \qquad \text{(S1.14)}$$

The contribution of the normal dissipative contact depends on the normal dashpot coefficient between the two particles, η_n, which is function of the normal restitution coefficient, and the normal relative velocity between the particles, which is computed by projecting the total relative velocity vector between the two particles at the contact point, V_s, on the unit vector η_c:

$$\boldsymbol{F}^{\boldsymbol{n}}{}_{\boldsymbol{D}} = \eta_n \left(\boldsymbol{V}_{\boldsymbol{s}} \cdot \boldsymbol{\eta}_{\boldsymbol{c}} \right) \boldsymbol{\eta}_{\boldsymbol{c}}. \tag{S1.15}$$

Similarly to the normal contacts, the tangential force may be split in conservative and dissipative terms:

$$\boldsymbol{F}_{\boldsymbol{C}}{}^{\boldsymbol{t}} = \boldsymbol{F}^{\boldsymbol{t}}{}_{\boldsymbol{S}} + \boldsymbol{F}^{\boldsymbol{t}}{}_{\boldsymbol{D}} \, . \tag{S1.16}$$

The first term on the right hand side is the conservative part of the tangential contact force (spring), and the second one is the dissipative part (dashpot). There are two ways to express the tangential spring, depending on the frictional state of the particle contact, which can be either static or dynamic. The static friction spring term is:

$$\boldsymbol{F}^{\boldsymbol{t}}{}_{\boldsymbol{S}} = -k_t \boldsymbol{\delta}_{\boldsymbol{t}}, \tag{S1.17}$$

where k_t is the tangential spring coefficient, and $\boldsymbol{\delta}_{\boldsymbol{t}}$ is the accumulated tangential displacement. The cumulated tangential displacement is computed during the 'static' frictional contact as:

$$\boldsymbol{\delta}_{\boldsymbol{t}} = \int_{static} \frac{\partial \boldsymbol{\delta}_{\boldsymbol{t}}}{\partial t} dt. \tag{S1.18}$$

To track the occurrence of tangential sliding (dynamic friction), a Mohr-Coulomb criterion is used. It assumes that the sliding occurs when the magnitude of the static tangential forces overcomes a threshold, that depends on the normal contact force $\boldsymbol{F}_{\boldsymbol{c}}^{\boldsymbol{n}}$ and particles friction coefficient, μ_s. Sliding is assumed to occur when:

$$\left\| \boldsymbol{F}^{\boldsymbol{t}}{}_{\boldsymbol{S}} \right\| > \mu_s \left\| \boldsymbol{F}_{\boldsymbol{C}}^{\boldsymbol{n}} \right\|. \tag{S1.19}$$

During sliding, the tangential force is given by:

$$\left\| \boldsymbol{F}^{\boldsymbol{t}}{}_{\boldsymbol{S}} \right\| = \mu_s \left\| \boldsymbol{F}_{\boldsymbol{C}}{}^{\boldsymbol{n}} \right\| \boldsymbol{t}, \tag{S1.20}$$

where, $\boldsymbol{t}$ is the tangential contact unit vector. When sliding occurs, the incremental evolution of the tangential displacement follows:

$$\boldsymbol{\delta}_{\boldsymbol{t}} = \frac{\mu_s k_n \delta_n}{k_t} \boldsymbol{t}. \tag{S1.21}$$

The tangential dashpot contribution is:

$$\boldsymbol{F}^{\boldsymbol{t}}_{\boldsymbol{D}} = \eta_t \left(\boldsymbol{V}_{\boldsymbol{s}} - \left(\boldsymbol{V}_{\boldsymbol{s}} \cdot \boldsymbol{\eta}_{\boldsymbol{c}} \right) \boldsymbol{\eta}_{\boldsymbol{c}} \right), \tag{S1.22}$$

where η_t is the tangential dashpot coefficient.

The total force exerted by the fluid to the solids includes both steady and unsteady terms:

$$\boldsymbol{F_{fs}} = \boldsymbol{F_P} + \boldsymbol{F_D} + \boldsymbol{F_{VM}} + \boldsymbol{F_B}. \quad \text{(S1.23)}$$

where, $\boldsymbol{F_P}$ is the pressure force vector, $\boldsymbol{F_D}$ is the viscous drag force vector, $\boldsymbol{F_{VM}}$ is the virtual mass force vector, and $\boldsymbol{F_B}$ is the Basset force vector. The first force describes the effect of the fluid pressure gradient. The drag expresses the steady viscous forces applied by the fluid on the particles (or vice versa) because of their relative motions. The two last forces are unsteady terms only important in transient dynamics that may be neglected in many cases including magma simulations (Burgisser et al, 2005). They both depend on the relative acceleration between the particles and the fluid. The virtual mass describes the effect of the force needed to move a volume of fluid when a particle is accelerating. The Basset term expresses the effect of the variation of the viscous boundary layer thickness (distance over which the fluid flow is affected by the presence of the particle). Neglecting the unsteady forces reduces the momentum transfer force to the drag and pressure terms:

$$\boldsymbol{F_P} + \boldsymbol{F_D} = -\left(\frac{\pi}{6} d_p^{\,3}\right) \nabla P - \frac{\beta}{(1-\Phi)} \left(\frac{\pi}{6} d_p^{\,3}\right) (\boldsymbol{v} - \boldsymbol{u}), \quad \text{(S1.24)}$$

where β is the momentum transfer coefficient, and d_p is the particle diameter. The pressure gradient may be decomposed in its hydrostatic and dynamic components. The dynamic part of the pressure forcce depends on the fluid motion. The hydrostatic pressure force is:

$$\boldsymbol{F_{Pstatic}} = \frac{-\pi}{6} d_p^{\,3} \rho_f \boldsymbol{g}, \quad \text{(S1.25)}$$

which corresponds to the Archimedes force. The drag coefficient is computed with the Gidaspow drag model, which presents the advantage to be valid over a wide range of concentrations in solids:

$$\beta = \begin{cases} \frac{3}{4} C_D \frac{\rho_f \Phi (1-\Phi) \|\boldsymbol{u} - \boldsymbol{v}\|}{d_p} (1-\Phi)^{-2.65} & if\ \Phi \le 0.2 \\ \frac{150 \Phi^2 \eta}{(1-\Phi) d_p^{\,2}} + \frac{1.75 \rho_f \Phi \|\boldsymbol{u} - \boldsymbol{v}\|}{d_p} & if\ \Phi > 0.2 \end{cases}. \quad \text{(S1.26)}$$

In equation S1.26, the upper line corresponds to the Wen-Yu drag coefficient and is valid for particle volume fractions below 0.2. Above 0.2, the Ergun law gives the coefficient of momentum transfer between the fluid and the particles, which is composed of two terms. The first corresponds to the viscous part and is given by a Kozeny-Carman relationship describing the viscous flow at low particle Reynolds numbers, Re_p. The second is the inertial term, which depends on the relative velocity between the two phases and comes from a Burke-Plummer equation, describing the fluid

kinetics at high Re_p. The Wen-Yu drag model requires to estimate the drag coefficient, C_D, for which empirical relationships exist with Re_p:

$$C_D = \begin{cases} \frac{24}{\mathrm{Re}_p}\left(1+0.15\,\mathrm{Re}_p^{\,0.687}\right), \\ 0.44 \end{cases} \tag{S1.27}$$

$$\mathrm{Re}_p = \frac{d_p \|\boldsymbol{u}-\boldsymbol{v}\| \rho_f}{\eta}. \tag{S1.28}$$

In case of viscous magmas $\mathrm{Re}_p < 1$ and $C_D = 24/\mathrm{Re}_p$. Because of the Newton's third law, the drag force exerted by the fluid on the particles must be taken into account within the interphases momentum transfer term in Eq. S1.2. The different numerical representations of the phases (Eulerian and Langrangian) impose at the drag force at the particle scale must be averaged in space to the fluid scale over a volume v_{REV}. This is also why the drag is a function of ϕ and involves a Kozeny-Carman relationship in Eq. (S1.26). Such parameterized drag takes into account the effect of the neighboring particles on the tortuosity of the fluid flow at high particle volume fraction by averaging the drag at the scale of the small particle aggregate contained in v_{REV}. The fluid-solid momentum exchange term may be expressed as:

$$\boldsymbol{I}_{\boldsymbol{fs}} = \frac{1}{v}\sum \left(\frac{\beta\left(\frac{\pi}{6} d_p^{\,3}\right)}{(1-\Phi)} (\boldsymbol{u}-\boldsymbol{v}) K_v(\boldsymbol{X}, \boldsymbol{X_f}) \right), \tag{S1.29}$$

with K_v being a generic kernel indicating the contribution of a particle located at a position $\boldsymbol{X}$ to a fluid grid node located at the position $\boldsymbol{X_f}$. The sum on the right hand side of Eq. S1.29 expresses the sum over all the particles comprised in the cells containing the fluid grid node located at $\boldsymbol{X_f}$.

To solve the fluid constitutive equations, MFIX-DEM uses the finite volume method and the SIMPLE (Semi-Implicit Method Linked Equations) algorithm (Patankar, 1980). It is an iterative method based on successive corrections of fluid velocities and pressure field. It uses a staggered grid in which fluid pressure and velocities are stored at different positions in order to avoid the convergence to checkerboard pressure fields. An overview of the algorithm steps is presented here. For a detailed presentation of the discretization of the constitutive equations and algorithm operations, see Patankar, 1980, and Syamlal, 1998. For each fluid time step, the algorithm operations are:

i: Update the fluid physical properties. Equations. S1.6 and S1.7 are used to compute the new densities and viscosities of the fluid according to the respective concentrations of the two melts.

ii. The velocity and pressure gradients are computed from the results of the previous iteration or time step (for the first iteration).

iii. The momentum equation (Eq. S1.2) is solved to compute a new velocity field with the pressure field from the previous iteration, (or a guessed one for the first solver's iteration). Note that the estimated velocity field generally does not respect the continuity equation (Eq. S1.1).

iv. The mass fluxes at each face of the control volumes are updated with the new fluid velocities field computed at step 3.

v. A fluid pressure correction is computed in order to obtain a pressure field satisfying the continuity equation (Eq. S1.1).

vi. The fluid pressure field is updated with the pressure correction from step 5.

vii. A fluid velocity correction is computed from the new pressure field.

viii. The total dynamic residual is computed by summing those of steps 3 and 5.

ix. If the total residual is below a threshold, the time step is considered as having converged and the fluid velocity, pressure, and temperature fields are used to compute the solids dynamics in the DEM part. If the total residual is above the threshold and converges (i.e. is smaller than that of the previous iteration), the algorithm restarts from step 2 with the fluid properties computed during the present iteration. If any residual diverges, the fluid time increment is reduced and the iteration is restarted from step 1 with the fluid properties from the previous time step.

Computing the particle motion requires one to integrate in time their accelerations given by Eqs. 1.8 and 1.9 and update their velocities and positions. For that, a first-order Euler time integration scheme is used (Gear, 1971). We also tested a second order scheme (Adams Bashforth) that we left aside because it did not change model outputs appreciably. The integral in time of the particles acceleration is thus approximated by:

$$\boldsymbol{v}(t+\Delta t)=\boldsymbol{v}(t)+\frac{\sum\left(\boldsymbol{F}_c\right)+\boldsymbol{F}_{fs}+m\boldsymbol{g}}{m}\Delta t. \tag{S1.30}$$

The positions of the particles are updated with:

$$\boldsymbol{X}(t+\Delta t)=\boldsymbol{X}(t)+\Delta t\,\boldsymbol{v}(t+\Delta t), \tag{S1.31}$$

where Δt_{solid} is the DEM time step. For the particle rotation, the Euler time integration is:

$$\boldsymbol{\omega}(t+\Delta t)=\boldsymbol{\omega}(t)+\frac{\sum \boldsymbol{T}_c}{I_s}\Delta t. \tag{S1.32}$$

To ensure stability of the simulations, the classical DEM integration scheme imposes to use time steps shorter than the characteristic duration of the physical processes controlling the crystal

motions, which are here contact durations and drag characteristic time. When increasing melt viscosity, the particle viscous response time, τ_v (time for the particle to adapt to changes in the fluid velocity) decreases, which results in short DEM time steps and impractically long computations. To accelerate the discrete model, we used the same approach as Burgisser et al. (2020) because the flows simulated are in the laminar regime and the particle Reynolds numbers are also well below the transition to turbulence (Furuichi and Nishiura, 2014). In the absence of particle contacts, the equation of motion for the solids reads:

$$\frac{d\boldsymbol{v}}{dt} = \frac{-\nabla P}{\rho_c} + \boldsymbol{g} + \frac{\beta}{\Phi \rho_p}(\boldsymbol{u} - \boldsymbol{v}), \tag{S1.33}$$

Similarly to Bergantz et al. (2017), the particle response time is defined as $\tau_v = \Phi \rho_p / \beta$. At low Reynolds and Stokes numbers, τ_v is shorter than the fluid characteristic time, which means that the fluid velocity and pressure gradient within Eq. (S1.33) may be considered constant during the acceleration of the particle in response to a change in its environment. Consequently, equation (S1.32) reduces to a first order ordinary differential equation having as solution:

$$\boldsymbol{v}(t) = \boldsymbol{v_0} e^{\frac{-t}{\tau_v}} + \left(\boldsymbol{u} + \tau_v\left(\boldsymbol{g} - \frac{\nabla P}{\rho_c}\right)\right)\left(1 - e^{\frac{-t}{\tau_v}}\right), \tag{S1.34}$$

where $\boldsymbol{v_0}$ is an initial particle velocity vector. The effective force, $\boldsymbol{F_{GPD}}$, needed to get from the velocity at time t_0 to that a DEM time step, Δt, later is:

$$\boldsymbol{F_{GPD}}(t_0) = \frac{m}{\Delta t}\left(\boldsymbol{v}(t_0 + \Delta t) - \boldsymbol{v}(t_0)\right), \tag{S1.35}$$

Setting $\boldsymbol{v_0} = \boldsymbol{v}(t)$ in Eq. (S1.34), $\boldsymbol{F_{GPD}}$ becomes:

$$\boldsymbol{F_{GPD}} = \frac{m}{\Delta t}\left(\boldsymbol{u}(t) + \tau_v\left(\boldsymbol{g} - \frac{\nabla P(t)}{\rho_p}\right) - \boldsymbol{v}(t)\right)\left(1 - e^{\frac{-\Delta t}{\tau_v}}\right), \tag{S1.36}$$

We implemented Eq. (S1.36) instead of MFIX's classical evaluations of the gravitational (Eq. S1.9), pressure and drag forces (Eq. S1.24), and left unchanged the computations of the contact forces and of the averaging of the drag forces exerted by the particles on the fluid.

S1.B Scaling of the numerical parameters against magmatic systems

Table S1a compares the range of physical parameters and dimensionless numbers used in the simulation against the ranges that may be encountered in natural magmatic systems.

Parameter	Range in simulations	Range estimated in nature
ρ_i (kg m^{-3})	2500	2200 – 2600
ρ_h (kg m^{-3})	2150 – 2550	2100 – 2600
ρ_c (kg m^{-3})	3300	2600 – 3500
ρ_{bh} (kg m^{-3})	2886 – 3012	2456 – 3140
W_{inj} (m)	0.1	0,01 – 10
U_{inj} (m s^{-1})	6.228×10^{-5} – 4.25	10^{-7} – 10
dp (m)	0.0045 – 0.0055	0.00001 – 0.05
η_i (Pa s)	1	0.1 – 1000
η_h (Pa s)	1 – 100	1 – 1×10^4
Re_i	0.0155 – 1062.5	2.2×10^{-10} – 2.6×10^4
Re_p	7×10^{-4} – 58.44	2.2×10^{-13} – 1300
At_m	-10^{-2} – 7.5×10^{-2}	-8.3×10^{-2} – 8.6×10^{-2}
At_b	-9.3×10^{-2} – -7.2×10^{-2}	-1.8×10^{-1} – 2.8×10^{-2}

Table S1a: Comparison of the range of physical parameters used in the simulations and the one encountered in natural magmatic systems. The bulk Atwood numbers are computed assuming that the intruder is crystal-free.

S1.C Model validation

S1.C.a Ability of the model to capture the mixing between two miscible fluids

To ensure that the numerical model is able to capture the interaction and possible mixing between two miscible fluids, we reproduced experiments involving two miscible fluids having distinct physical properties (density and viscosity).

We reproduced first the experiment from Séon et al. (2007). The experiment was performed in a tube filled with two miscible fluids having the same viscosity and different densities. The denser fluid was located at the top half of the tube and the lighter one at the bottom half. The tube is then tilted by a certain angle from the vertical. The experiment started once the gate separating the two fluids was opened. Séon et al. (2007) identified two regimes they called “diffusive spreading”, in which the respective concentrations of the two fluids tend to a median value following a classic diffusion law, and “Non-diffusive spreading”, in which the mixing between the two fluids is dominated by interface deformation due to a combination of Rayleigh-Taylor (at initiation) and Kelvin-Helmholtz (during flowage) instabilities (Fig S1a). If our implementation of two fluids (Eq. S1.5-1.8) is subject to excessive numerical diffusion, or incorrectly represents buoyancy forces the

fluids exert of each other, we expect that the numerical runs cannot capture the difference between these two regimes.

We performed one numerical experiment for each regime using the same fluid properties and tilt angle as those used by the authors. Figure S1b displays snapshots of the simulation in the "diffuse spreading" regime. Simulation shows a good transverse mixing between the two fluids as expected from the experiment. Figure S1c shows snapshots of the second simulation standing in the "non-diffuse spreading" regime. Here, the simulation presents a poor lateral mixing between the two fluids that is dominated by the diffusion of the local concentrations of C_h and C_i towards 0.5. This successful reproduction of the two regimes validates the ability of the model to capture the interaction and mixing between two miscible fluids having different densities but the same viscosity.

To ensure that the model captures properly the dynamics of two miscible fluids having distinct densities and viscosities, we reproduced a series of 8 experiments performed by Snyder & Tait (1995). Experiment setup consists in a 100-cm long, 40-cm hight, and 30-cm wide tank filled with a host fluid in which another fluid is injected through a slot having a width of 2 cm. The injected fluid is denser and less viscous than the host one. We used the same domain size, fluid properties, and injection flux as the authors in their experiments (Table S1b). Based on the experimental results, the theoretical current height is (Snyder and Tait, 1995):

$$h(t)=1.8\left(\frac{\eta_i t Q_{inj}^{\ 2}}{\|g\|(\rho_i-\rho_h)}\right)^{\frac{1}{5}}, \tag{S1.37}$$

where Q_{inj} is the injection flux, and g the magnitude of the gravitational acceleration. As equation S1.37 depends on time, we compared the theoretical and modeled current heights at a given dimensionless time, t', defined as:

$$t'=\frac{W_{inj}}{U_{inj}}, \tag{S1.38}$$

where W_{inj} is the injection width, and U_{inj} is the superficial injection velocity. At t', the theoretical current height is:

$$h(t')=1.8\left(\frac{\eta_i t' U_{inj}}{W_{inj}W^2\|\boldsymbol{g}\|(\rho_i-\rho_h)}\right)^{\frac{1}{5}}, \tag{S1.39}$$

where W is the tank width. The current velocity, U_{front}, may be predicted as (Snyder and Tait, 1998) :

$$U_{front}=\frac{dl}{dt}=0{,}43\left(\frac{\|\boldsymbol{g}\|(\rho_i-\rho_h)Q_{inj}^{\ 3}}{\eta_h}\right)^{\frac{1}{3}}. \tag{S1.40}$$

We compared the current height above the inlet at a given time, *t'*=50, at which the gravity currents were well developed in our simulations. In the simulations, the current velocities also evolved with time. In order to compare the numerical and theoretical velocities, we used the average current front velocity measured during the simulation.

Figure S1d displays the comparison of the theoretical and modeled current heights and velocities. All simulations show good agreement between simulated currents and those predicted from the experiments. In the experiments, flow front instabilities occurred. Whether with (main text) or without (this Supplementary material) particles, we never observed such instabilities in our simulations. This absence most likely results from the size of the fluid cells, which were too large to initiate the Rayleigh-Taylor instability of the 1–2 cell-thick host liquid film trapped underneath the injected current. Despite tour obstinately stable flow fronts, the good match in current characteristics between the numerical experiments and theory shows that the model is able to model the gravity currents dynamics of two miscible fluids of contrasted densities and viscosities.

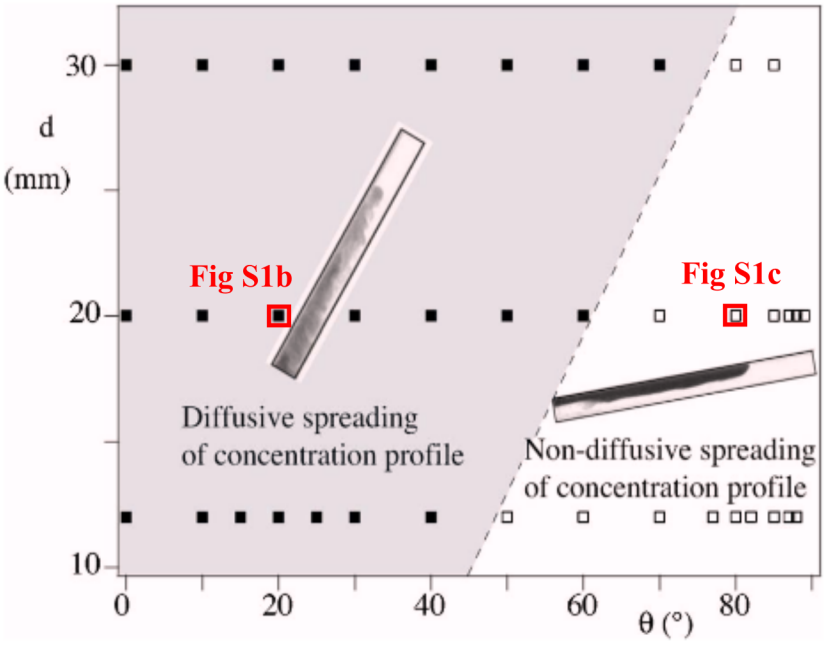

Figure S1a: Regime diagram of the dynamics of two miscible fluids having different densities (reproduced from Séon et al, 2007). Each black square represents an experiment. Its color depends on the flow regime observed. The black color indicates that the experiment was in the diffusive spreading regime and a white color indicates that the experiment was characterized by a non-diffusive spreading regime. The two red squares locate the two simulations we performed. The dashed line delineates the transition between the two regimes.

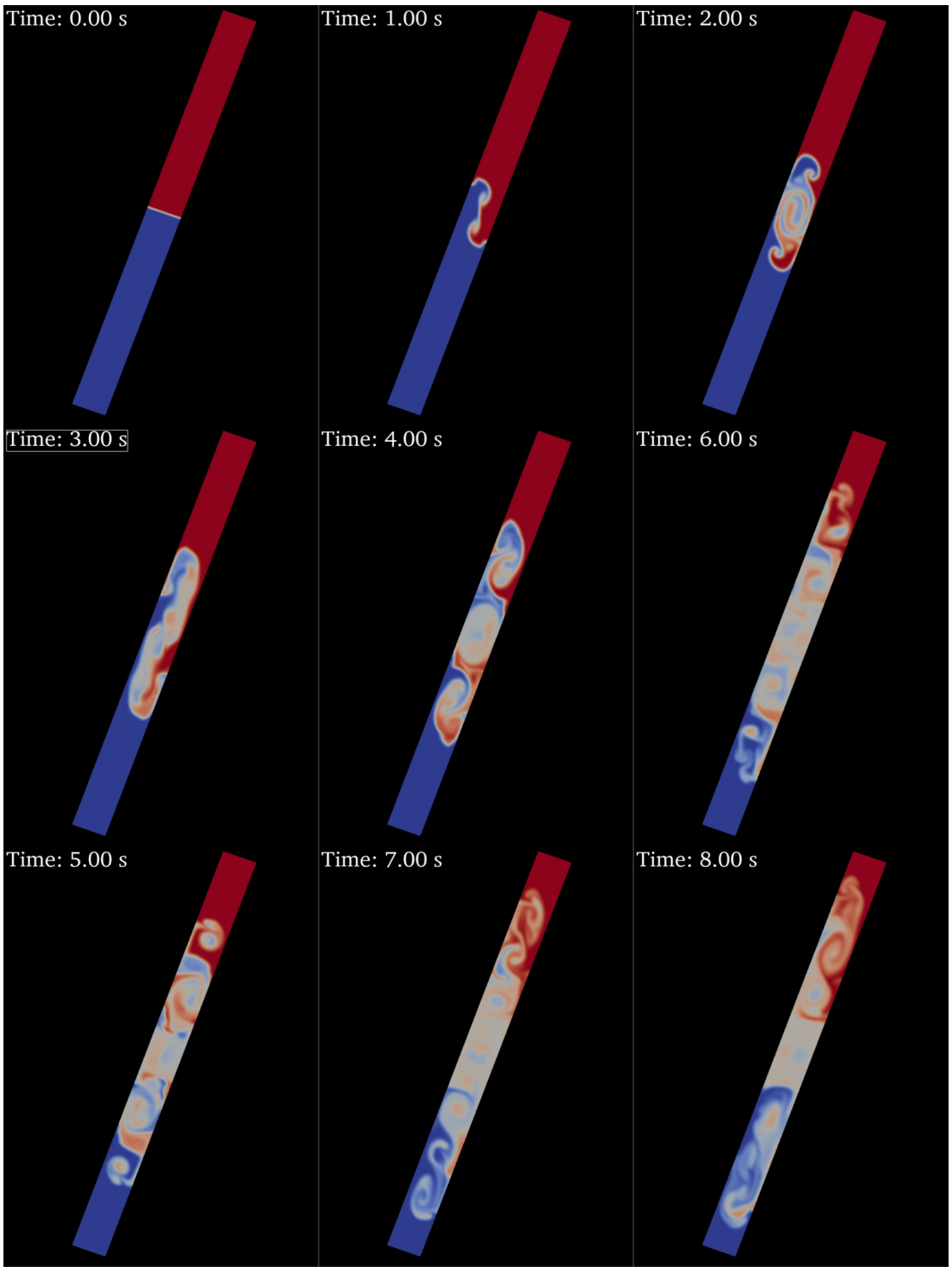

Figure S1b: Snapshots of the numerical simulation reproducing the diffuse regime in Séon et al, (2007). The simulation is performed in 2D domain measuring 50 by 2 cm. The domain is tilted by 20° from the vertical. The color depends on the local concentration between the two fluids. The fluid in blue has a density of 1000 kg m^{-3} and the one in red a density of 1020 $kg.m^{-3}$. Both fluids have a dynamic viscosity of 10^{-3} Pa s.

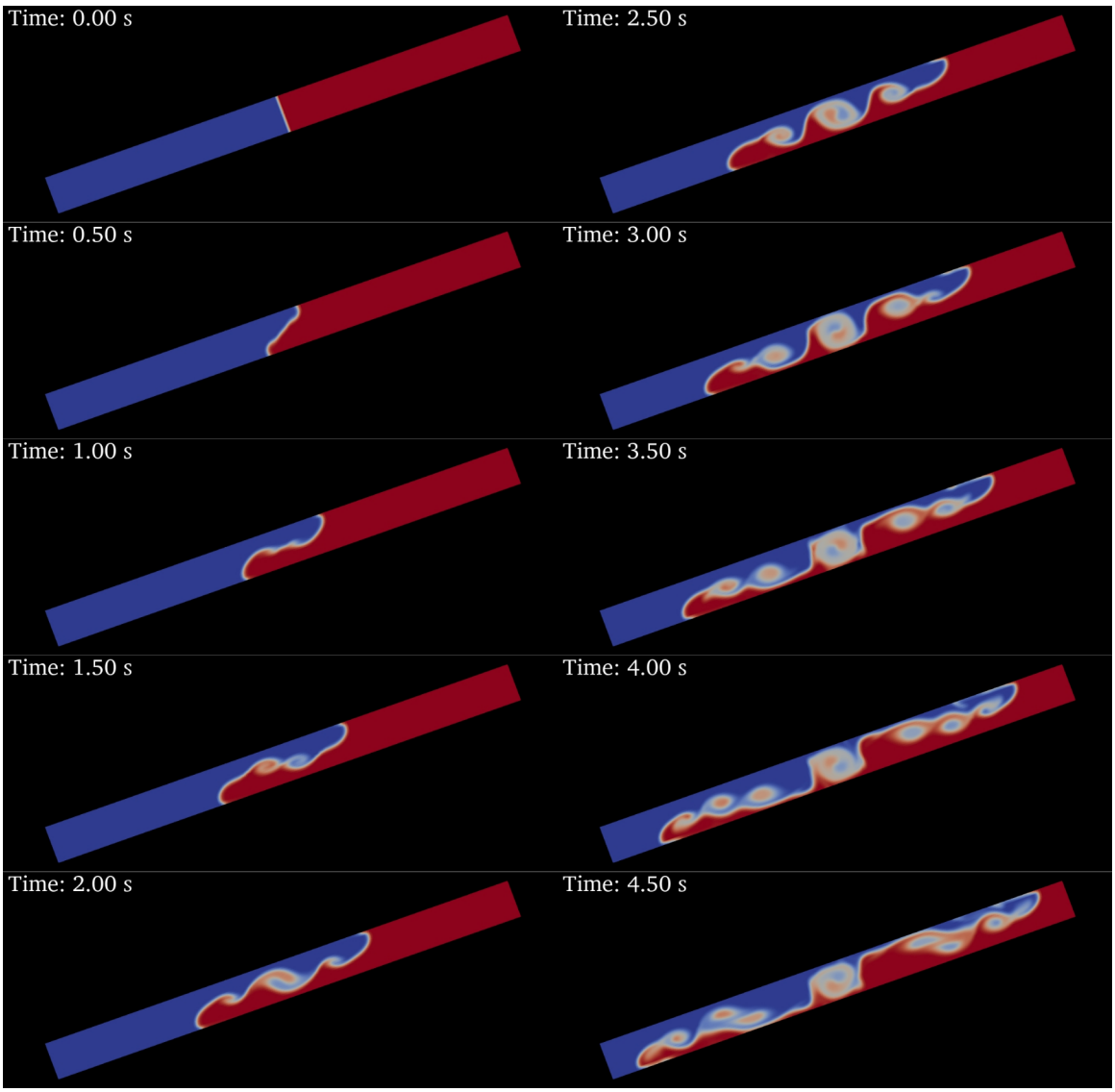

Figure S1c: Snapshots of the numerical simulation reproducing the non-diffuse regime in Séon et al, (2007). The numerical domain and fluids are the same as in Fig. S1b. The domain is tilted by 80° from the vertical

Run	Experiment n°	ρ_i (kg m^{-3})	ρ_h (kg m^{-3})	η_i (Pa s)	η_h (Pa s)	Q_{inj} (m^3 s^{-1})	U_{inj} (m s^{-1})	t at t'=50 (s)	h at t'=50 (cm)	U_{front} (m s^{-1})	h obs (cm)	u_front obs
1	5	1024	1000	0.083	10.3	$9.39\ 10^{-5}$	$1.57\ 10^{-2}$	60	5.35	$2.52\ 10^{-3}$	5.22	$3.64\ 10^{-3}$
2	1	1051	1000	0.33	10.3	$3.57\ 10^{-5}$	$5.95\ 10^{-3}$	160	3.80	$1.70\ 10^{-3}$	3.64	$2.01\ 10^{-3}$
3	7	1025	1000	1.8	27	$7.97\ 10^{-6}$	$1.38\ 10^{-3}$	750	3.7	$3.58\ 10^{-4}$	3.96	$4.20\ 10^{-4}$
4	10	1011	1000	2.3	40	$1.60\ 10^{-5}$	$2.67\ 10^{-3}$	370	5.81	$3.80\ 10^{-4}$	6.37	$5.16\ 10^{-3}$
5	41	1428	1401	0.26	5	$2.81\ 10^{-5}$	$4.68\ 10^{-3}$	210	3.58	$1.49\ 10^{-3}$	3.43	$1.58\ 10^{-3}$
6	39	1012	1000	0.05	0.19	$9.63\ 10^{-5}$	$1.61\ 10^{-2}$	60	2.79	$7.70\ 10^{-3}$	2.42	$7.83\ 10^{-3}$
7	40	1012	1000	0.05	0.19	$1.49\ 10^{-4}$	$2.48\ 10^{-2}$	40	3.07	$1.03\ 10^{-2}$	2.92	$1.06\ 10^{-2}$
8	24	1051	1001	1.2	2.1	$3.12\ 10^{-5}$	$5.2\ 10^{-3}$	190	2.72	$2.62\ 10^{-3}$	3.19	$2.22\ 10^{-3}$

Table S1b: List of the experiment reproduced numerically and associated physical parameters. The dimensionless time t' was computed using Eq. S1.38. The current height and velocity were

estimated using the relationships given in Snyder and Tait (1995), and Snyder and Tait (1998) (Eqs S1.39–40).

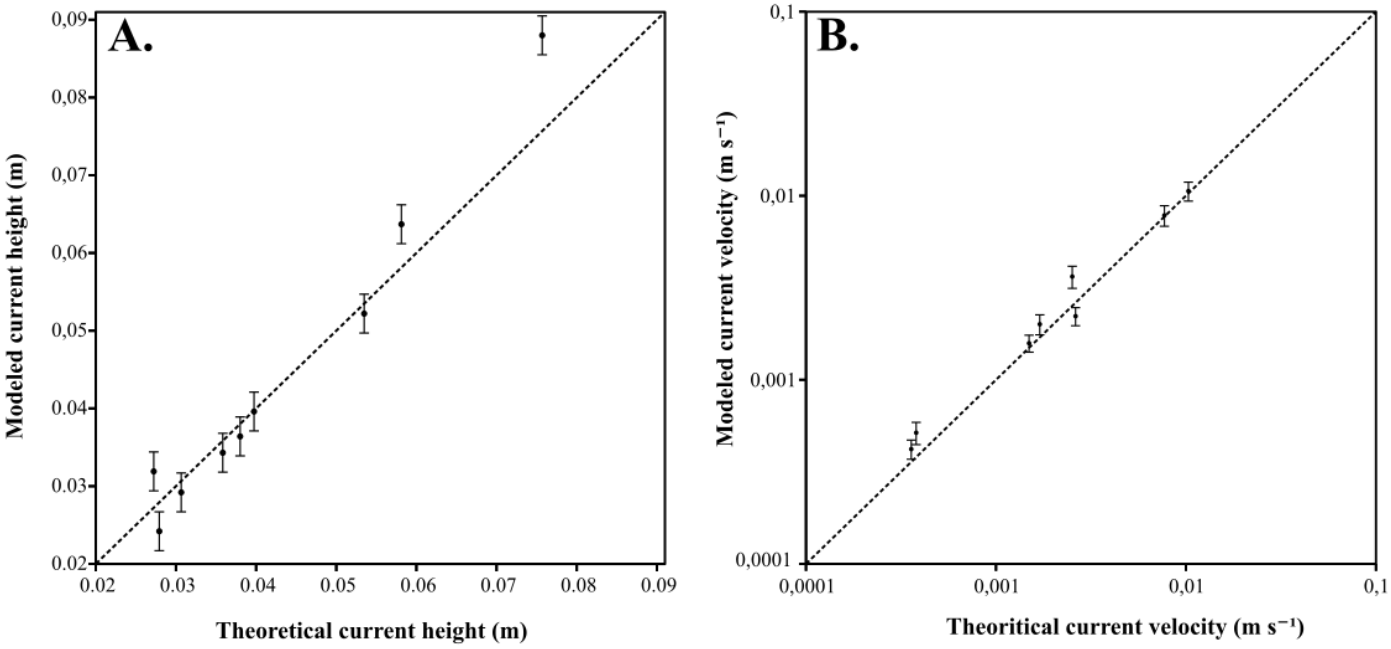

Figure S1d: Comparison of theoretical and modeled gravity currents. **[A]** Comparison of the theoretical (Eq. S1.39) and modeled current height. Heights were measured in simulations at a dimensionless time t'=50 (Eq. S1.38) above the inlet. The dashed line indicates, perfect match between theoretical and modeled current height. Each point corresponds to a simulation. The error on the measurement of the current height is taken as ± half a cell size. **[B]** Same as (A) for the comparison of the theoretical (Eq. S1.40) and modeled current velocity. The error on the measurement is ± the ratio of half the cell size and the time intervals at which the current lengths were measured.

S1.C Spatial resolution of the melt

The fluid grid resolution greatly affects CFD-DEM simulations and can have a larger impact than the drag law used (Beetstra et al., 2007) as it controls at which scale the particle volume fraction is computed in the fluid cells and its spatial standard deviation. Volk et al. (2018), showed that the error against experimental data is minimized when the grid size is between 2 and 6 times larger than the Sauter mean diameter of the particles ($dp_{Sauter} = (\int dp^3 / \int dp^2)$). In our case with 3 distinct but close diameters, the Sauter mean diameter is almost equal to the median diameter used. Bellow the critical cell size ($dx=2\ dp$), the assumption made in unresolved CFD-DEM that the medium can be considered as a continuum becomes invalid, the solid volume fraction becoming

more heterogeneous and highly dependent on the position of each particle. For lower grid resolution than the optimal one, the difference against experimental results diverges as the cell size reduces (Volk et al., 2018). On the contrary, when resolution of the fluid grid become larger than 6 *dp*, the error against experiments increases with the gird size, as the model become unable to capture the spatial fluctuation of the drag force.

The comparison between fully resolved models and CFD-DEM has been performed by Esteghamatian et al. (2018, 2017). Esteghamatian et al. (2017) showed that CFD-DEM models are able to capture fairly well the macroscopic behavior of particle-rich flows such as the particle bed height and pressure drop between the inlet and top of the bed. At a smaller scale, however, the CFD-DEM approach is no able to properly capture the local microstructure and the fluctuation in the velocity of the particles observed with fully-resolved models, especially in the transverse direction. This also decreases the magnitude of the contact forces between the particles. As expected, the fluid velocity field is smoother when using a CFD-DEM approach, resulting in the absence of fluctuation in the fluid velocity field at the particle scale. Esteghamatian et al. (2018) proposed to add a stochastic fluctuating term in the drag law. As demonstrated by the authors, this approach tends to make the CFD-DEM simulations closer to the fully resolved cases. This approach, however, requires a calibration against fully-resolved simulations, which are very costly. One can expect that when $Re << 1$, the characteristic length of the fluid are much larger than the size of the particles and fluctuations in the fluid flow field at the particles scale become negligible. Under this assumption, the CFD-DEM approach is thus likely to provide results very close to fully-resolved one.

S1.D Equations

This Supplementary Information includes two tables summarizing the equation system solved in our numerical simulations (Tables S1c–S1d).

Table S1c: List of the equations implemented in the CFD-DEM model

Equation names	Equations	Ref.
Mass conservation	$\frac{\partial(1-\Phi)}{\partial t}+\nabla\cdot\left((1-\Phi)\boldsymbol{u}\right)=0$	1
Momentum conservation	$\rho_f\left(\frac{\partial}{\partial t}\left((1-\Phi)\boldsymbol{u}\right)+\nabla\cdot\left((1-\Phi)\boldsymbol{u}\otimes\boldsymbol{u}\right)\right)=\nabla\cdot\left(\underline{\underline{\boldsymbol{\sigma}_v}}\right)+(1-\Phi)\rho_f\boldsymbol{g}+\boldsymbol{I_{fs}}$	1
Stress tensor	$\underline{\underline{\boldsymbol{\sigma}_f}}=P\,\underline{\underline{\boldsymbol{\delta}_{ij}}}+\frac{2}{3}\eta\,tr\left(\underline{\underline{\boldsymbol{\epsilon}_f}}\right)\underline{\underline{\boldsymbol{\delta}_{ij}}}+2\eta\,\underline{\underline{\boldsymbol{\epsilon}_f}}$	1
Euler velocity integration	$\boldsymbol{v}^{(k)}(t+\Delta t)=\boldsymbol{v}^{(k)}(t)+\Delta t\,\frac{\boldsymbol{F_{GPD}}^{(k)}(t)+\sum_{l=1}^{N_l^{(k)}}\left(\boldsymbol{F_C^n}^{(k,l)}(t)+\boldsymbol{F_C^t}^{(k,l)}(t)\right)}{m^{(k)}}$	Eq. (4.4)
Euler displacement integration	$\boldsymbol{X}^{(k)}(t+\Delta t)=\boldsymbol{X}^{(k)}(t)+\Delta t\,\boldsymbol{v}^{(k)}(t+\Delta t)$	2
Euler rotation integration	$\boldsymbol{\omega}^{(k)}(t+\Delta t)=\boldsymbol{\omega}^{(k)}(t)+\Delta t\,\frac{\sum_{l=1}^{N_l^{(k)}}\boldsymbol{T_C}^{(k,l)}}{I^{(k)}}$	2
Normal contact force	$\boldsymbol{F_c^n}^{(i,j)}=-k_n^{(i,j)}\delta_n^{(i,j)}\boldsymbol{\eta_c}^{(i,j)}+\eta_n^{(i,j)}\boldsymbol{V_S}^{(i,j)}$	2 5
Tangential contact force	$\boldsymbol{F_c^T}^{(i,j)}=-k_t^{(i,j)}\boldsymbol{\delta_t^{(i,j)}}+\eta_t^{(i,j)}\left(\boldsymbol{V_S}^{(i,j)}-\left(\boldsymbol{V_S}^{(i,j)}.\boldsymbol{\eta_c^{(i,j)}}\right)\boldsymbol{\eta_c^{(i,j)}}\right)$	2 5
Collisional torque	$\boldsymbol{T_c}^{(i,j)}=\frac{d_p^{(i)}-\delta_n^{(i,j)}}{2}\boldsymbol{F_c^t}^{(i,j)}$	2
normal spring (Hertzian model)	$k_n^{(i,j)}=\frac{4}{3}\frac{E^{(i)}E^{(j)}\sqrt{R_{eff}^{(i,j)}}}{E^{(j)}\left(1-\sigma^{(i)2}\right)+E^{(i)}\left(1-\sigma^{(j)2}\right)}\delta_n^{(i,j)\frac{1}{2}}$	2
tangential spring (Hertzian model)	$k_t^{(i,j)}=\frac{16}{3}\frac{G^{(i)}G^{(j)}\sqrt{R_{eff}^{(i,j)}}}{G^{(j)}\left(2-\sigma^{(i)}\right)+G^{(i)}\left(2-\sigma^{(j)}\right)}\left\|\boldsymbol{\delta_t^{(i,j)}}\right\|^{\frac{1}{2}}$	2
Elastic modulus	$G=\frac{E}{2(1+\sigma)}$	2
Normal damping coefficient	$\eta_n^{(i,j)}=\frac{2\sqrt{m_{eff}^{(i,j)}k_n^{(i,j)}}\left\lvert\ln e_n\right\rvert}{\sqrt{\pi^2+\ln^2 e_n}}\delta_n^{(i,j)\frac{1}{4}}$	2 5
Tangential damping coefficient	$\eta_t^{(i,j)}=\frac{2\sqrt{m_{eff}^{(i,j)}k_t^{(i,j)}}\left\lvert\ln e_t\right\rvert}{\sqrt{\pi^2+\ln^2 e_t}}\left\|\boldsymbol{\delta_t}\right\|^{(i,j)\frac{1}{4}}$	2 5
effective radius	$R_{eff}^{(i,j)}=\frac{2\left(d\left\lvert p^{(i)}+d_p^{(j)}\right.\right)}{d_p^{(i)}d_p^{(j)}}$	2
Effective mass	$m_{eff}^{(i,j)}=\frac{m^{(i)}+m^{(j)}}{m^{(i)}m^{(j)}}$	2
Solids/Fluid momentum exchange on REV	$\boldsymbol{I_{fs}}=\frac{1}{v}\sum\left(\frac{\beta\left(\frac{\pi}{6}{d_p}^3\right)}{(1-\Phi)}(\boldsymbol{u}-\boldsymbol{v})K_v(\boldsymbol{X},\boldsymbol{X_f})\right)$	2

Equation names	Equations	Ref.
Drag forces (for the fluid)	$\boldsymbol{F}_{\boldsymbol{D}}^{(k)} = -\nabla P\left(\frac{\pi}{6} d_p^{(k)3}\right) + \frac{\beta_{fs}^{(k)}}{\left(1-\left(1-\Phi\right)\right)}\left(\frac{\pi}{6} d_p^{(k)3}\right)\left(\boldsymbol{u}-\boldsymbol{v}^{(k)}\right)$	2
Local fluid/solid momentum transfer	$\beta_{fs}^{(k)} = \begin{cases} \frac{3}{4} C_D^{(k)} \frac{\rho_f \left(1-\Phi\right)\Phi \left\|\boldsymbol{u}-\boldsymbol{v}^{(k)}\right\|}{d_p^{(k)}} \left(1-\Phi\right)^{-2.65} & if\ \Phi \le 0.2 \\ \frac{150\Phi^2\eta}{\left(1-\Phi\right) d_p^{(k)2}} + \frac{1.75\,\rho_f \Phi \left\|\boldsymbol{u}-\boldsymbol{v}^{(k)}\right\|}{d_p^{(k)}} & if\ \Phi_f > 0.2 \end{cases}$	3 4
Drag coefficient	$C_D^{(k)} = \begin{cases} \frac{24}{\mathrm{Re}^{(k)}\left(1+0.15\,\mathrm{Re}^{(k)0.687}\right)} & if\ \mathrm{Re}^{(k)} < 1000 \\ 0.44 & if\ \mathrm{Re}^{(k)} \ge 1000 \end{cases}$	3 4
Particle Gravity-Drag-Pressure force	$\boldsymbol{F}_{\boldsymbol{GPD}} = \frac{m}{\Delta t}\left(\boldsymbol{u} + \tau_v\left(\boldsymbol{g} - \frac{\nabla P}{\rho_p}\right) - \boldsymbol{v}\right)\left(1 - e^{\frac{-\Delta t}{\tau_v}}\right)$	Eq. (4.5)
Reynolds number	$\mathrm{Re}^{(k)} = \frac{d_p^{(k)} \left\|\boldsymbol{u}-\boldsymbol{v}^{(k)}\right\| \rho_f}{\eta}$	3

[1] Syamlal et al., (1993)
[2] Garg et al., (2010)
[3] Benyahia et al., (2012)
[4] Gidaspow, (1986)

Table S1d: Symbols used in Table S1c

Symbol	Definition
$C_D^{(k)}$	Drag coefficient of the kth particle
$d_p^{(i)}$	ith particle diameter
e_n	Particle normal restitution coefficient
e_t	Particle tangential restitution coefficient
$E^{(i)}$	ith particle Young modulus
$\boldsymbol{F}_C^{n(k,l)}$	Normal contact force between kth particle and its lth neighbor
$\boldsymbol{F}_C^{t(k,l)}$	Tangential contact forces between kth particle and its lth neighbor
$\boldsymbol{F}_D^{(k)}$	Drag force on kth particle
$\boldsymbol{g}$	Gravitational vector
$G^{(k)}$	kth particle shear moduli
$\boldsymbol{I}_{fs}$	Fluid-solid momentum exchange
$I^{(k)}$	kth particle moment of inertia
K_{REM}	Generic kernel to determine the influence of a particle located at $X^{(k)}$ on the REV
$k_n^{(i,j)}$	Normal spring coefficient between ith and jth particles contact
$k_t^{(i,j)}$	Tangential spring coefficient between ith and jth particles contact
l	Neighbors index
$m^{(k)}$	kth particle mass
$m_{eff}^{(i,j)}$	ith and jth particles effective mass
$N_l^{(k)}$	Number of neighbors of the kth particle
N_k	Number of particles
P	Fluid pressure
REV	Representative elementary volume
$\mathrm{Re}^{(k)}$	ith particle Reynolds number
$R_{eff}^{(i,j)}$	ith and jth particles effective radius
$\boldsymbol{T}_C^{(k,l)}$	Contact torque between kth particle and its lth neighbor
$\boldsymbol{u}$	Fluid velocity vector
$\boldsymbol{v}^{(k)}$	kth particle velocity vector
$\boldsymbol{X}^{(k)}$	kth particle position
$\beta_{fs}^{(k)}$	kth particle – fluid momentum transfer coefficient
$\boldsymbol{V}_S^{(i,j)}$	Normal relative velocity between ith and jth particles
$\underline{\underline{\boldsymbol{\delta_{ij}}}}$	Kronecker tensor
$\delta_n^{(i,j)}$	Normal overlap between ith and jth particles
$\boldsymbol{\delta}_t^{(i,j)}$	Tangential displacement during the contact between ith and jth particles contact
$\underline{\underline{\boldsymbol{\epsilon}_f}}$	Fluid strain rate tensor
η	Fluid viscosity
$\boldsymbol{\eta}_c^{(i,j)}$	Normal vector between between ith and jth particles
$\eta_n^{(i,j)}$	Normal damping coefficient between ith and jth particles
$\eta_t^{(i,j)}$	Tangential damping coefficient between ith and jth particles
v	Domain volume
ρ_f	Fluid density
$\sigma^{(i)}$	ith particle Poisson coefficient

$\underline{\underline{\sigma_f}}$	Fluid stress tensor
Φ	Particle volume fraction
$\omega^{(k)}$	k[th] particle rotation vector

Supplementary Information 2:

This supplementary information presents an updated derivation of the minimum fluidization velocity compared to those used in the literature.

The onset of fluidization of a crystal bed occurs when the upward drag force exerted by the injected fluid exceed its net weight. Shi et al. (1984) proposed a formula to predict the minimum fluidization velocity of a random packed bed due to a localized injection of fluid. These authors made the assumption that the fluid velocity is only vertical and uniformly distributed on horizontal cross-sectional area (Fig. S2a). The total upward drag force is computed with the Ergun's formula (Ergun, 1952) for a bed fluidized uniformly. Later, Cui et al. (2014) adapted this formula by considering the fluid velocity uniform along a semi-circular cross sectional area. Here, we modify the approach of Cui et al. (2014) to predict the minimum fluidization velocity in the experimental apparatus geometry because the original derivation incorrectly assumed the distance between the injection point and center of the inlet, r_0 , and the boundaries of the integral in their Eq. (2.13).

The total upward drag force applied by the inlet on the particle bed is computed as:

$$F_D = \int_{r_0}^{H+r_0} \left(A U_r + B U_r^2\right) S(r)\, dr, \tag{S2.1}$$

where r_0 correspond of the vertical coordinates of the bottom and $H+r_0$ is the position of the top of the particle bed. The variable r corresponds to the radial distance from a hypothetic injection point (Fig. S2a). A and B are given by Ergun (1952):

$$A = 150 \frac{\phi^2}{(1-\phi)^3} \frac{\eta_f}{d_p^2}, \tag{S2.2}$$

$$B = 1.75 \frac{\phi}{(1-\phi)^3} \frac{\rho_f}{d_p}. \tag{S2.3}$$

$S(r)$ represents the area of the curved surface on which the fluid velocity is uniform, and it is computed as a function of r as:

$$S(r) = 2\alpha(r) W_l. \tag{S2.4}$$

U_r is the fluid velocity at a radial distance r. U_r may be computed by considering that the injected flux is conserved through the particle bed height, which yields:

$$Q_{inj} = U_r S(r), \tag{S2.5}$$

and, with (S4):

$$U_r = \frac{Q_{inj}}{2\alpha (r + r_0) W_l} \tag{S2.6}$$

Substituting Eqs. (S2.6) and (S2.4) into Eq. (S2.1) yields:

$$F = A Q_{inj} H_0 + \frac{B Q_{inj}^{\ 2}}{2\alpha W_l} \ln\left(\frac{H_0 + 2r_0}{2r_0}\right) \tag{S2.7}$$

In this geometry, the net weight of the bed, W, is given by:

$$W = \left[(r_0 + H_0)^2 \tan\alpha - \frac{W_{inj} r_0}{2}\right] W_l (\rho_p - \rho_f) g \phi. \tag{S2.8}$$

Introducing $r_0 = W_{inj}/(2\tan\alpha)$, the onset of fluidization occurred when $F = W$, which yields:

$$A Q_{inj} H_0 + \frac{B Q_{inj}^{\ 2}}{2\alpha W_l} \ln\left(\frac{2H_0 \tan\alpha}{W_{inj}} + 1\right) - \left[H_0 (W_{inj} + H_0 \tan\alpha)\right] W_l (\rho_p - \rho_f) g \phi = 0 \tag{S2.9}$$

Figure S2b displays comparison of the minimum fluidization velocities computed with formulas from Ergun (1952), Shi et al. (1984), Cui et al., (2014), and Eq. (S2.9), function of the particle bed height. It shows that Eq (S2.9) is closer to the result predicted with the formulas from Ergun (1952) and Shi et al. (1984). The incorrect formula derived by Cui et al., (2014) results in the significant overestimations of the minimum fluidization velocity.

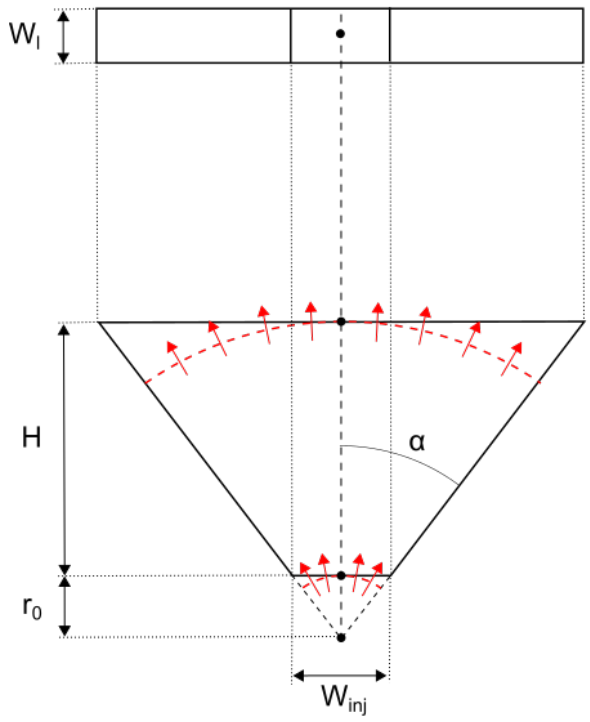

Figure S2a: Conceptual framework to derive the minimum fluidization velocity. The top

draw is a view from the top. The bottom draw is a front view. On both draws, the thick black lines represent the boundaries of the volume of the particle bed, which is fluidized. The red dashed curves indicate the cross sectional areas where the magnitude of the fluid velocity is uniform. The arrows represent the direction of the fluid flow. The black dots represent the positions of the theoretical injections point and intersections between the cross sectional areas where the fluid velocity is uniform and the vertical boundary of the fluidized particle bed**.**

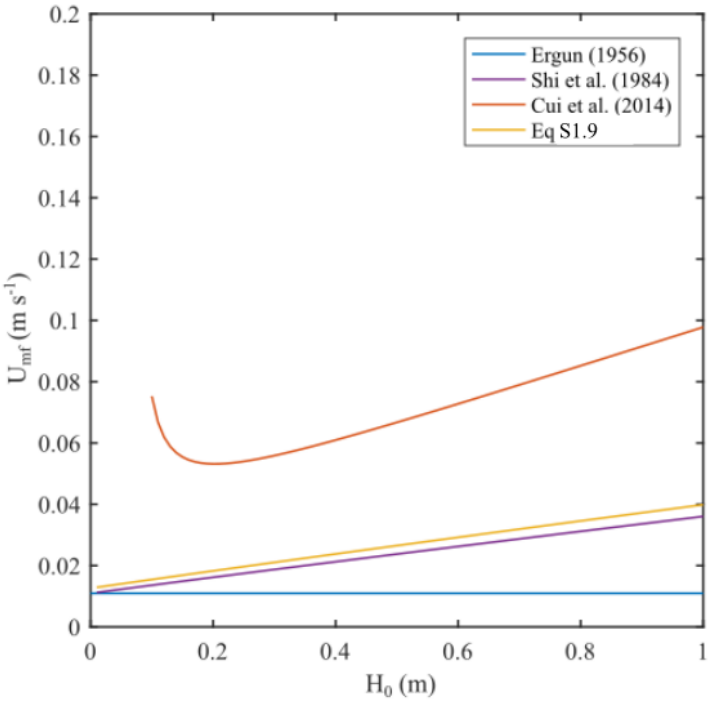

Figure S2b: Comparison of the minimum fluidization velocities function of the initial particle bed height. The curves represent the minimum fluidization velocities derived by authors and the one given here.

Supplementary Information 3:

This supplementary information presents the derivation of the maximum height of the intrusion as a function of time for end member scenarios.

We consider two end-members for the growth of the intrusion volume (vertical or radial). The first end member considers the vertical ascent (dyking) of the intruded melt above the inlet over a width, W_{inj}. In this case, the ratio, $H^{\square}$, between H_{max} and the initial particle bed thickness, H_{bed} ($H^{*}=H_{max}/H_{bed}$), reads:

$$H^{*}=t^{*}. \tag{S3.1}$$

In the case of radial growth, we consider as spherical intrusion having a unknown radius, R, and fed by an inlet of width W_{inj} (Fig. S3a). The inlet truncates the sphere at a vertical distance, h, which depends on both R and W_{inj}. The objective is to compute the distance from the inlet to the top of the sphere, H, knowing the area A and injection width W_{inj}. The total area, A_{tot}, of the sphere is the sum of the area A, where the intruded fluid is present and the truncated area B as:

$$A_{tot}=A+B. \tag{S3.2}$$

The area A depends on injection velocity and time. The area A_{tot} may be expressed using the sphere radius R. Replacing A and A_{tot} in Eq. (S3.2) and rearranging yields:

$$\pi R^{2}=W_{inj}H_{bed}t^{*}+A_{B}. \tag{S3.3}$$

The area B may be approximated with a good accuracy as (Harris and Stöcker, 1998, pp 92-93):

$$A_{B}\approx\frac{2}{3}W_{inj}h+\frac{h^{3}}{2W_{inj}}\ . \tag{S3.4}$$

Inserting Eq. (S3.4) in Eq. (S3.3) gives:

$$0=W_{inj}H_{bed}t^{*}+\frac{2}{3}W_{inj}h+\frac{h^{3}}{2W_{inj}}-\pi R^{2}. \tag{S3.5}$$

Equation (S3.5) contains two unknowns, R and h, which can be related to each other tanks to geometry:

$$0=\frac{W_{inj}{}^{2}}{4}+(R-h)^{2}-R^{2}. \tag{S3.6}$$

Using that $H=2R-h$, H_{max} may be computed as a function of t^{*} by solving Equations (S3.5–S3.6).

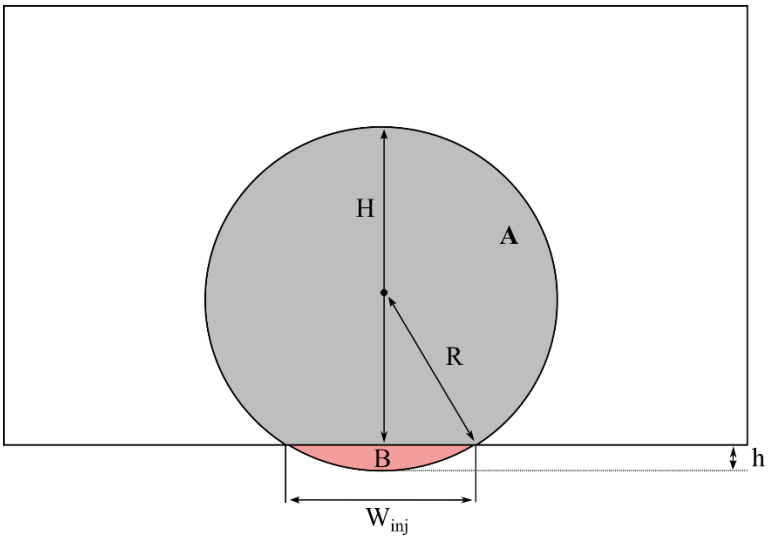

Figure S3a: Schematics of the geometrical setup. The drawing represents a section perpendicular to the intrusion. The area covered by the injected melt is in gray and the area outside the tank is red.

Supplementary information 4:

This supplementary figure displays the magnitude of the vorticity.

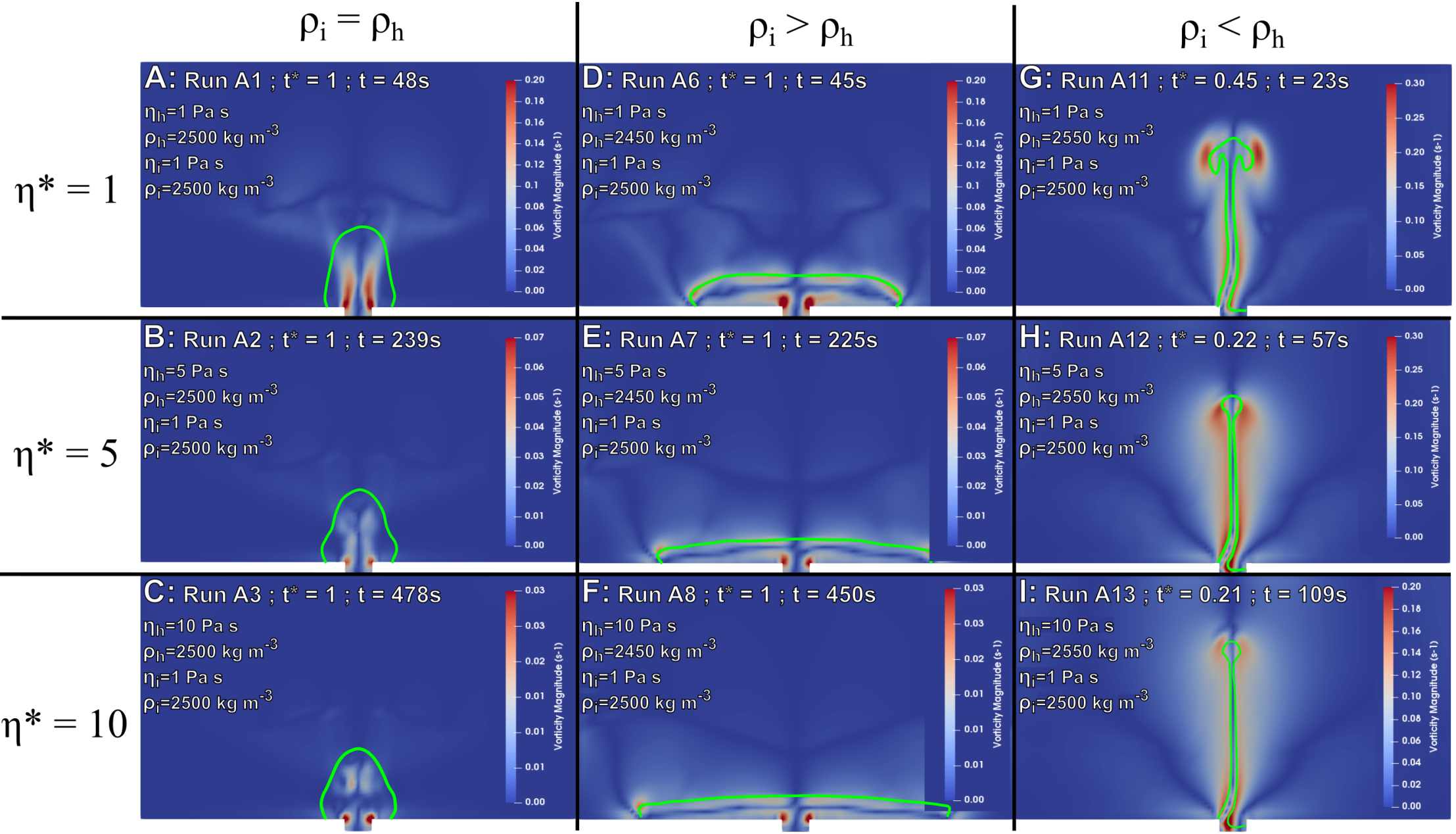

Figure S4a: Magnitude of the vorticity. Simulations correspond to the ones represented in Fig. 3 at the same time steps. The green curves indicate the injected melt contour.

Supplementary information 5:

This supplementary section present the physical properties of the end member magmas involved in the 15 eruptions considered in this study. In cases where mixing was so preeminent that only mixed products were erupted (e.g., Unzen), pre-mixing host characteristics, including crystal content, were determined using indirect evidences such as crystal rims in disequilibrium with the surrounding melt. Viscosities and densities of intruder magmas were sometimes directly characterized because they were erupted (e.g., Pinatubo; Pallister et al., 1996) or approximated using petrological inferences. The software Conflow (Mastin, 2002) was used to calculate densities and viscosities when necessary.

All host magmas are mushes except two complex cases treated separately in our analysis. The first case is the Bronze Age eruption of Santorini volcano known as the Minoan eruption. In one scenario, the reservoir that hosted the Minoan eruption products had 10–20 vol% crystals (Cadoux et al., 2014). In others, more complex scenarios have been proposed (Druitt, 2014; Flaherty et al., 2018; Martin et al., 2010). In one, the main rhyodacite would have instead acted as the intruder into an adjacent mushy, mafic reservoir (Druitt, 2014). For simplicity, we only reported the possibility of a mushy mafic reservoir. The 1912 eruption at Katmai–Novarupta is a case where the roles of the intruder and host might be reversed (e.g. Coombs and Gardner, 2001; Eichelberger and Izbekov, 2000; Hammer et al., 2002; Singer et al., 2016). We reported the scenario in which the most crystal-rich components (andesite and dacite) are the hosts and the nearly aphyric rhyolite is the intruder (Eichelberger and Izbekov, 2000), as well as the scenario in which the host is composed of a zoned chamber and the intruder is a basaltic andesite (Singer et al., 2016).

There is a last complex case that is analyzed individually although its reservoir unambiguously contained a mush. Two mutually exclusive intrusion scenarios have indeed been proposed to explain the 1991–1995 eruption of Unzen volcano. In both scenarios, the host magma was a phenocryst-rich,

low-temperature rhyolite mush and the intruder was a nearly aphyric, high-temperature magma (Holtz et al., 2004; Nakamura, 1995). The composition of the intruder, which left only cryptic indications of its presence such as reverse zoning of the outer rims of hornblende, plagioclase and magnetite (Nakamura, 1995), could have been either andesitic (Holtz et al., 2004), or basaltic (Browne et al., 2006).

Table S5a: Host properties from natural cases (volcano names are followed by the starting year of the eruption). Minerals abbreviations are plagioclase (Plag), clinopyroxene (CPx), orthopyroxene (OPx), pyroxene (Px), and hornblende (Hb). Only the main mineral phases were taken into account and numbers in parenthesis are mineral volume proportions. Bulk densities were calculated with a plagioclase density of 2570 kg/m^3 and a density of 3200 kg/m^3 for all other minerals. Bulk viscosities were calculated as $\eta_l(1-\varphi/0.6)^{-2.5\cdot 0.6}$, where η_l is melt viscosity and φ is crystal volume fraction, except for the Minoan scenario where the largest bulk viscosity was capped at 10^{10} Pa s because the higher bound of φ is >0.6. Abbreviations sat. and usat. mean saturated and undersaturated, respectively. Not used (n.u.) implies that melt densities and/or viscosities were directly given in the reference(s) corresponding to that case.

CASE	Name	Xtal (vol%)	Minerals	Melt SiO_2 (wt%)	Melt H_2O (wt%)	Melt density (kg/m^3)	Melt viscosity (Pa s)	T (°C)	P (MPa)	Ref
Unzen 1991	Dacite	34-35	Plag (0.8) Cpx (0.2)	75	8	2229-2239	1.3×10^4-1.4×10^4	775	300	1
Vesuvius -79	White Pumice	31.6-40	Plag	53-57	sat.	2218-2300	2.4×10^3-3.0×10^3	875-900	150 [b]	2
Guadeloupe 1530	Andesite	48.3-57.5	Plag (0.8) Px (0.2)	73-75	5.5-6	2189-2203	1.2×10^4-2.5×10^4	825-875	135-200	3
Karymsky 1996	Andesite	25-32	Plag (0.8) Px (0.2)	63	sat.	2395-2378 [a]	8.9×10^3-13×10^3 [a]	1023-1057	200 [b]	4
Ruapehu 1995	Andesite	24.5-42	Plag (0.66) Px (0.33)	62-70	1-1.5	2380-2438	2.9×10^4-4.7×10^4	920-1030	40	5
Katmai 1912 – scenario 1	Andesite	30-45	Plag (0.8) Px (0.2)	67.6-74	usat-sat.	2274-2284	1.2×10^4-1.3×10^4	920-970	75-120	6
	Dacite	30-45	Plag (0.8) Px (0.2)	79.1	usat-sat.	2189-2220	2.0×10^5-8.1×10^5	850-910	60-25	
Katmai 1912 – scenario 2	Andesite	30	Plag (0.8) Px (0.2)	67.6	usat.	2274	1.2×10^4	920	75	7
	Rhyolite	2	Plag	77	4	2225	1.7×10^6	790	40	
Komagatake 1640	White Pumice	25-43.1	n.u.	74.7-76.1	3-4	2280-2300	4.4×10^4-2.9×10^5 [a]	970-980	n.u.	8
Montserrat 1995	Andesite	35-45	Plag	75-80	4.8	2171-2160	3.7×10^4-8.4×10^4	835-880	105-155	9
Redoubt 1990	Dacite	24-32	Plag	78.5-81	4	2164-2174	3.4×10^4-3.8×10^4	840-950	100	10
Minoan	Andesite	55-100	Plag (0.8) CPx (0.2)	71-77	sat. [b]	2213-2231	5.9×10^5-1.3×10^7	700-820	50	11
SW Trident 1953	Dacite	37-39	Plag (0.8) Px (0.2)	75	3.6	2190-2200	4.5×10^4-4.9×10^4	890	90	12
Dutton 1989	Dacite	35	Plag (0.8) OPx (0.2)	78	sat.	2481-2491	1.4×10^5-1.5×10^5	865	200 [b]	13
Pinatubo 1991	White Pumice	47	Plag (0.8) Hb (0.2)	76	6-6.5	2166	5.4×10^4	750-800	155-200	14
	Tan Pumice	15-26	Plag (0.8) Hb (0.2)	73	6-6.5	2194	5.6×10^4	750-800	155-200	

[a] Calculated from bulk values given in the reference(s).

[b] Assumed value.

[c] References are: 1) Holtz et al. (2005), Vetere et al. (2008)(andesite intruder), Browne et al. (2006)(basalt intruder); 2) Cioni et al. (1995), Scaillet et al. (2008); 3) Pichavant et al. (2018); 4) Izbekov et al. (2002), Izbekov et al. (2004), Eichelberger and Izbekov (2000); 5) Nakagawa et al. (1999), Nakagawa et al. (2002), Kilgour et al. (2013); 6) Eichelberger and Izbekov (2000), Coombs and Gardner (2001); 7) Hammer et al. (2002), Singer et al. (2016); 8) Takahashi and Nakagawa (2013); 9) Barclay et al. (1998),

Murphy et al. (2000), Couch et al. (2001), Humphreys et al. (2010), Plail et al. (2018); 10) Wolf and Eichelbeger (1997), Nye et al. (1994), Swanson et al. (1994); 11)Druitt et al. (1999) 12) Coombs et al. (2000), Coombs et al. (2002); 13) Miller et al. (1999); 14) Pallister et al. (1992), Pallister et al. (1996), Bernard et al. (1996).

Table S5b: Intruder properties from natural cases. Minerals abbreviations are plagioclase (Plag), clinopyroxene (CPx),, pyroxene (Px), hornblende (Hb), olivine (Ol), and Augite (Aug). Abbreviations and references are the same as in Table S5a.

CASE	Name	Xtal (vol%)	Minerals	Melt SiO_2 (wt%)	Melt H_2O (wt%)	Melt density (kg/m^3)	Melt viscosity (Pa s)	T (°C)	P (MPa)
Unzen 1991	Andesite	0-10	Plag [b]	62-64	4	2184-2194	3.2×10^2-3.2×10^2	1030-1130	300
	Basalt	0-5	Ol	50	sat. [b]	2351-2418	2.3-10	1030-1200 [b]	300 [b]
Vesuvius -79	K-rich basalt	0-20	Plag	50-52	usat.	2485-2441	13-16	1050-1140	150 [b]
Guadeloupe 1530	Basalt	0-12	Plag	50-53	5-6	2436-2420	5.4-9.3	975-1025	200 [b]
Karymsky 1996	Basalt	20	Plag	52	sat.	2545 [a]	22-54	1080-1115	200 [b]
Ruapehu 1995	High-T magma	0-10	Plag [b]	54.2-57.7	1-1.5	2530-2640	10-10^2	1100 [b] -1200 [b]	40
Katmai 1912 – scenario 1	Rhyolite	2	Plag	77	4	2225-2172	7.5×10^3-1.7×10^6	790-850	40-100
Katmai 1912 – scenario 2	Andesite	30-45	Plag (0.8) Px (0.2)	67.6-74	usat.-sat.	2274-2284	1.2×10^4-1.3×10^4	920-970	75-120
Komagatake 1640	Basalt	0		57	n.u.	2500 [b]-2540	5.0×10^3-1.0×10^3 [a]	1150	n.u.
Montserrat 1995	Mafic recharge	2-4.5	Plag	52-71	sat.	2400-2500	10-10^2	975-1196	105-155
Redoubt 1990	Andesite	24-32	Plag	64.5-66	4	2228-2238	1.6×10^4-1.8×10^4	840-950	100
Minoan	Rhyodacite	10-20	Plag	73.5-74	5-6	2213-2173	1.7×10^4-1.4×10^5	845-860	200-250
SW Trident 1953	Andesite	28-43	Plag	74-63	3.5	2150-2295	8.3×10^2-10^4	990-1010	90
Dutton 1989	Mafic recharge	10-30	Plag	74	sat.	2546-2556	80-88	1080-1180	200 [b]
Pinatubo 1991	Basalt	19-25	Plag (0.75) Hb+Aug+Ol (0.25)	73.2	2-3 usat.	2159-2169	6.1×10^2-6.7×10^2	1250	250

[a] Calculated from bulk values given in the reference(s).
[b] Assumed value.

Supplementary references:

Barclay, J., Rutherford, M.J., Carroll, M.R., Murphy, M.D., Devine, J.D., Gardner, J., Sparks, R.S.J., 1998. Experimental phase equilibria constraints on pre-eruptive storage conditions of the Soufriere Hills magma. Geophys. Res. Lett. 25, 3437–3440.

Beetstra, R., van der Hoef, M.A., Kuipers, J.A.M., 2007. Numerical study of segregation using a new drag force correlation for polydisperse systems derived from lattice-Boltzmann simulations. Chemical Engineering Science 62, 246–255.

Benyahia, S., Syamlal, M., O'Brien, T.J., 2012. Summary of MFIX equations 2012-1. URL Httpsmfix Netl Doe GovdocumentationMFIXEquations2012-1 Pdf.

Bergantz, G.W., Schleicher, J.M., Burgisser, A., 2017. On the kinematics and dynamics of crystal-rich systems. J. Geophys. Res. Solid Earth 122, 2017JB014218. https://doi.org/10.1002/2017JB014218

Bernard, A., Knittel, U., Weber, B., Weis, D., Albrecht, A., Hattori, K., Klein, J., Oles, D., 1996. Petrology and geochemistry of the 1991 eruption products of Mount Pinatubo (Luzon, Philippines) 1126.

Browne, B.L., Eichelberger, J.C., Patino, L.C., Vogel, T.A., Dehn, J., Uto, K., Hoshizumi, H., 2006a. Generation of Porphyritic and Equigranular Mafic Enclaves During Magma Recharge Events at Unzen Volcano, Japan. J. Petrol. 47, 301–328. https://doi.org/10.1093/petrology/egi076

Browne, B.L., Eichelberger, J.C., Patino, L.C., Vogel, T.A., Uto, K., Hoshizumi, H., 2006b. Magma mingling as indicated by texture and Sr/Ba ratios of plagioclase phenocrysts from Unzen volcano, SW Japan. J. Volcanol. Geotherm. Res., Modern Trends in Petrography: 154, 103–116. https://doi.org/10.1016/j.jvolgeores.2005.09.022

Burgisser, A., Bergantz, G.W., Breidenthal, R.E., 2005. Addressing complexity in laboratory experiments: the scaling of dilute multiphase flows in magmatic systems. J. Volcanol. Geotherm. Res. 141, 245–265. https://doi.org/10.1016/j.jvolgeores.2004.11.001

Burgisser, A., Carrara, A., Annen, C., 2020. Numerical simulations of magmatic enclave deformation. J. Volcanol. Geotherm. Res. 392, 106790. https://doi.org/10.1016/j.jvolgeores.2020.106790

Cadoux, A., Scaillet, B., Druitt, T.H., Deloule, E., 2014. Magma Storage Conditions of Large Plinian Eruptions of Santorini Volcano (Greece). J. Petrol. 55, 1129–1171. https://doi.org/10.1093/petrology/egu021

Cioni, R., Civetta, L., Marianelli, P., Metrich, N., Santacroce, R., Sbrana, A., 1995. Compositional layering and syn-eruptive mixing of a periodically refilled shallow magma chamber: the AD 79 Plinian eruption of Vesuvius. J. Petrol. 36, 739–776.

Coombs, M.L., Eichelbeger, J.C., Rutherford, M.J., 2000. Magma storage and mixing conditions for the 1953-74 eruptions of Southwest Trident volcano, Katmai National Park, Alaska. Contrib. Mineral. Petrlogy 140, 99–118.

Coombs, M.L., Eichelberger, J.C., Rutherford, M.J., 2002. Experimental and textural constraints on mafic enclave formation in volcanic rocks. J. Volcanol. Geotherm. Res. 119, 125–144.

Coombs, M.L., Gardner, J.E., 2001. Shallow-storage conditions for the rhyolite of the 1912 eruption at Novarupta, Alaska. Geology 29, 775–778.

Couch, S., Sparks, R.S.J., Carroll, M.R., 2001. Mineral disequilibrium in lavas explained by convective self-mixing in open magma chambers. Nature 411, 1037–1039.

Cui, X., Li, J., Chan, A., Chapman, D., 2014. Coupled DEM–LBM simulation of internal fluidisation induced by a leaking pipe. Powder Technol. 254, 299–306. https://doi.org/10.1016/j.powtec.2014.01.048

Druitt, T.H., 2014. New insights into the initiation and venting of the Bronze-Age eruption of Santorini (Greece), from component analysis. Bull. Volcanol. 76, 794. https://doi.org/10.1007/s00445-014-0794-x

Druitt, T.H., Edwards, L., Mellors, R.M., Pyle, D.M., Sparks, R.S.J., Lanphere, M., Davies, M., Barreirio, B., 1999. Santorini Volcano. Geol. Soc. Mem. 19, 165.

Eichelberger, J.C., Izbekov, P.E., 2000. Eruption of andesite triggered by dyke injection: contrasting cases at Karymsky Volcano, Kamchatka and Mt Katmai, Alaska. Philos. Trans. RS Lond. A358, 1465–1485.

Ergun, S., 1952. Fluid flow through packed columns. Chem Eng Prog 48, 89–94.

Esteghamatian, A., Bernard, M., Lance, M., Hammouti, A., Wachs, A., 2017. Micro/meso simulation of a fluidized bed in a homogeneous bubbling regime. International Journal of Multiphase Flow 92, 93–111.

Esteghamatian, A., Euzenat, F., Hammouti, A., Lance, M., Wachs, A., 2018. A stochastic formulation for the drag force based on multiscale numerical simulation of fluidized beds. International Journal of Multiphase Flow 99, 363–382.

Flaherty, T., Druitt, T.H., Tuffen, H., Higgins, M.D., Costa, F., Cadoux, A., 2018. Multiple timescale constraints for high-flux magma chamber assembly prior to the Late Bronze Age eruption of Santorini (Greece). Contrib. Mineral. Petrol. 173, 75. https://doi.org/10.1007/s00410-018-1490-1

Furuichi, M., Nishiura, D., 2014. Robust coupled fluid-particle simulation scheme in Stokes-flow regime: Toward the geodynamic simulation including granular media. Geochem. Geophys. Geosystems 15, 2865–2882. https://doi.org/10.1002/2014GC005281

Garg, R., Galvin, J., Li, T., Pannala, S., 2010. Documentation of open-source MFIX–DEM software for gas-solids flows. URL Httpsmfix Netl Doe Govdocumentationdemdoc2012-1 PdfAccessed 31 March 2014.

Gear, C., 1971. Simultaneous Numerical Solution of Differential-Algebraic Equations. IEEE Trans. Circuit Theory 18, 89–95. https://doi.org/10.1109/TCT.1971.1083221

Gidaspow, D., 1986. Hydrodynamics of Fiuidizatlon and Heat Transfer: Supercomputer Modeling. Appl. Mech. Rev. 39, 1–23. https://doi.org/10.1115/1.3143702

Hammer, J.E., Rutherford, M.J., Hildreth, W., 2002. Magma storage prior to the 1912 eruption at Novarupta, Alaska. Contrib. Mineral. Petrol. 144, 144–162.

Harris, J.W., Stöcker, H., 1998. Handbook of Mathematics and Computational Science. Springer-Verlag, New York.

Holtz, F., Sato, H., Lewis, J., Behrens, H., Nakada, S., 2005. Experimental petrology of the 1991-1995 Unzen dacite, Japan. Part I. Phase relations, phase composition and pre-eruptive conditions. J. Petrol. 46, 319–337.

Holtz, F., Sato, H., Lewis, J., Behrens, H., Nakada, S., 2004. Experimental petrology of the 1991–1995 Unzen dacite, Japan. Part I: phase relations, phase composition and pre-eruptive conditions. Journal of petrology 46, 319–337.

Ishii, M., Hibiki, T., 2011. Thermo-Fluid Dynamics of Two-Phase Flow. Springer Science+Business Media , LLC ,.

Izbekov, P., Gardner, J.E., Eichelberger, J.C., 2004. Comagmatic granophyre and dacite from Karymsky volcanic center, Kamchatka: experimental constraints for magma storage conditions. J. Volcanol. Geotherm. Res. 131, 1–18.

Izbekov, P.E., Eichelberger, J.C., Patino, L.C., Vogel, T.A., Ivanov, B.V., 2002. Calcic cores of plagioclase phenocrysts in andesite from Karymsky volcano: Evidence for rapid introduction by basaltic replenishment. Geology 30, 799–802. https://doi.org/10.1130/0091-7613(2002)030<0799:CCOPPI>2.0.CO;2

Kilgour, G., Blundy, J., Cashman, K., Mader, H.M., 2013. Small volume andesite magmas and melt–mush interactions at Ruapehu, New Zealand: evidence from melt inclusions. Contrib. Mineral. Petrol. 166, 371–392. https://doi.org/10.1007/s00410-013-0880-7

Martin, V.M., Davidson, J., Morgan, D., Jerram, D.A., 2010. Using the Sr isotope compositions of feldspars and glass to distinguish magma system components and dynamics. Geology 38, 539–542. https://doi.org/10.1130/G30758.1

Mastin, L.G., 2002. Insights into volcanic conduit flow from an open-source numerical model. Geochem. Geophys. Geosystems 3, 1–18. https://doi.org/10.1029/2001GC000192

Miller, T.P., Chertkoff, D.G., Eichelberger, J.C., Coombs, M.L., 1999. Mount Dutton volcano, Alaska: Aleutian arc analog to Unzen volcano, Japan. J. Volcanol. Geotherm. Res. 89, 275–301.

Murphy, M.D., Sparks, R.S.J., Barclay, J., Carroll, M.R., Brewer, T.S., 2000. Remobilization of andesite magma by intrusion of mafic magma at the Soufriere Hills Volcano, Montserrat, West Indies. J. Petrol. 41, 21–42.

Nakagawa, M., Wada, K., Thordarson, T., Wood, C.P., Gamble, J.A., 1999. Petrologic investigations of the 1995 and 1996 eruptions of Ruapehu volcano, New Zealand: formation of discrete and small magma pockets and their intermittent discharge. Bull. Volcanol. 61, 15–31.

Nakagawa, M., Wada, K., Wood, C.P., 2002. Mixed magmas, mush chambers and eruption triggers: Evidence from zoned clinopyroxene phenocrysts in andesitic scoria from the 1995 eruptions of Ruapehu volcano, New Zealand. J. Petrol. 43, 2279–2303.

Nakamura, M., 1995. Continuous mixing of crystal mush and replenished magma in the ongoing Unzen eruption. Geology 23, 807–810.

Nye, C.J., Swanson, S.E., Avery, V.F., Miller, T.P., 1994. Geochemistry of the 1989-1990 eruption of Redoubt volcano: Part I. Whole-rock major- and trace-element chemistry. J. Volcanol. Geotherm. Res. 62, 429–452.

Pallister, J.S., Hoblitt, R.P., Meeker, G.P., Knight, R.J., Siems, D.F., 1996. Magma mixing at Mount Pinatubo: petrographic and chemical evidence from the 1991 deposits. pp. 687–731.

Patankar, S.V., 1980. Numerical heat transfer and fluid flow. Hemisphere Pub. Corp.

Pichavant, M., Poussineau, S., Lesne, P., Solaro, C., Bourdier, J.-L., 2018. Experimental Parametrization of Magma Mixing: Application to the ad 1530 Eruption of La Soufrière, Guadeloupe (Lesser Antilles). J. Petrol. 59, 257–282. https://doi.org/10.1093/petrology/egy030

Plail, M., Edmonds, M., Woods, A.W., Barclay, J., Humphreys, M.C.S., Herd, R.A., Christopher, T., 2018. Mafic enclaves record syn-eruptive basalt intrusion and mixing. Earth Planet. Sci. Lett. 484, 30–40. https://doi.org/10.1016/j.epsl.2017.11.033

Scaillet, B., Pichavant, M., Cioni, R., 2008. Upward migration of Vesuvius magma chamber over the past 20,000 years. Nature 455, 216–220.

Séon, T., Znaien, J., Perrin, B., Hinch, E.J., Salin, D., Hulin, J.P., 2007. Front dynamics and macroscopic diffusion in buoyant mixing in a tilted tube. Phys. Fluids 19, 125105. https://doi.org/10.1063/1.2821733

Shi, Y.F., Yu, Y.S., Fan, L.T., 1984. Incipient fluidization condition for a tapered fluidized bed. 484–489.

Singer, B.S., Costa, F., Herrin, J.S., Hildreth, W., Fierstein, J., 2016. The timing of compositionally-zoned magma reservoirs and mafic 'priming' weeks before the 1912 Novarupta-Katmai rhyolite eruption. Earth Planet. Sci. Lett. 451, 125–137. https://doi.org/10.1016/j.epsl.2016.07.015

Snyder, D., Tait, S., 1998. The imprint of basalt on the geochemistry of silicic magmas. Earth Planet. Sci. Lett. 160, 433–445. https://doi.org/10.1016/S0012-821X(98)00102-2

Snyder, D., Tait, S., 1995. Replenishment of magma chambers: comparison of fluid-mechanic experiments with field relations. Contrib. Mineral. Petrol. 122, 230–240. https://doi.org/10.1007/s004100050123

Swanson, S.E., Nye, C.J., Miller, T.P., Avery, V.F., 1994. Geochemistry of the 1989-1990 eruption of Redoubt volcano: Part II. Evidence from mineral and glass chemistry. J. Volcanol. Geotherm. Res. 62, 453–468.

Syamlal, M., Rogers, W., OBrien, T.J., 1993. MFIX documentation theory guide. USDOE Morgantown Energy Technology Center, WV (United States).

Syamlal, M., 1998. MFIX documentation numerical technique. EG and G Technical Services of West Virginia, Inc., Morgantown, WV (United States).

Takahashi, R., Nakagawa, M., 2013. Formation of a Compositionally Reverse Zoned Magma Chamber: Petrology of the ad 1640 and 1694 Eruptions of Hokkaido-Komagatake Volcano, Japan. J. Petrol. 54, 815–838. https://doi.org/10.1093/petrology/egs087

Tsuji, Y., Kawaguchi, T., Tanaka, T., 1993. Discrete particle simulation of two-dimensional fluidized bed. Powder Technol. 77, 79–87. https://doi.org/10.1016/0032-5910(93)85010-7

Vetere, F., Behrens, H., Schuessler, J.A., Holtz, F., Misiti, V., Borchers, L., 2008. Viscosity of andesite melts and its implication for magma mixing prior to Unzen 1991–1995 eruption. J. Volcanol. Geotherm. Res., Scientific drilling at Mount Unzen 175, 208–217. https://doi.org/10.1016/j.jvolgeores.2008.03.028

Volk, A., Ghia, U., Liu, G.R., 2018. Assessment of CFD-DEM solution error against computational cell size for flows through a fixed-bed of binary-sized particles. Powder Technology 325, 519–529.

Wolf, K.J., Eichelbeger, J.C., 1997. Syneruptive mixing, degassing, and crystallization at Redoubt Vocano, eruption of December, 1989 to May 1990. J. Volcanol. Geotherm. Res. 75, 19–37.